Front. Optoelectron. 2013, 6(1): 3–24
DOI 10.1007/s12200-012-0301-y

REVIEW ARTICLE

Photonic crystal fibers, devices, and applications

Wei JIN (✉), Jian JU, Hoi Lut HO, Yeuk Lai HOO, Ailing ZHANG

Department of Electrical Engineering, The Hong Kong Polytechnic University, Hong Kong, China

Abstract This paper reviews different types of air-silica photonic crystal fibers (PCFs), discusses their novel properties, and reports recent advances in PCF components and sensors as well as techniques for splicing PCFs to standard telecomm fibers.

Keywords photonic crystal fibers (PCFs), microstructured optical fibers, hollow-core photonic bandgap fibers (HC PBFs), optical fiber devices, optical fiber sensors

1 Introduction

Photonic crystal fibers (PCFs) are optical fibers that have wavelength-scale morphological microstructure running along their length [1]. They, according to their guiding mechanisms, may be divided into index-guiding (IG)-PCFs [2] and photonic bandgap fibers (PBFs) [3].

In IG-PCFs, light is confined to a solid core by modified total internal reflection (M-TIR) from a reduced-effective-index cladding formed by an array of air-holes within a glass or polymer matrix. Figure 1 shows a few examples of air-silica IG-PCFs. They are endlessly single mode PCF (Fig. 1(a)) [2] that support only the fundamental mode over the entire wavelength range, highly nonlinear PCF (Fig. 1(b)) [4] that has a very small core size and novel dispersion characteristics, and highly birefringent (Hi-Bi) PCFs (Fig. 1(c)) [5]. Similar to the conventional silica optical fibers, IG-PCFs have broad transmission windows from below 500 nm to beyond 1800 nm.

In PBFs, light is confined to a lower index (e.g., air) core by reflection from the photonic crystal (PC) cladding. A typical hollow-core (HC) PBF is shown in Fig. 2(a), where an air-core is surrounded by an inner PC cladding comprising of a triangular array of air-holes in a silica background. Since the air-core has a lower refractive index than silica, TIR guidance of light in the core is not possible. However, the PC cladding processes 2D off-plane photonic bandgaps (PBGs) [3], within which light transmission in the transverse plane is prohibited. Within a PBG of the PC cladding, it acts as a high reflectivity mirror to confine light in the hollow core. Compared with IG-fibers, PBFs have relatively narrower transmission bands (Fig. 2(b)) with sharp loss edges corresponding to the band edges of the cladding PBGs. The center wavelength and the width of the transmission band are affected by the pitch (i.e., spacing between the holes) and size of the air-hole cladding lattice.

In the following sections, we review the properties of single and two-mode (TM) PCFs, Hi-Bi PCFs, highly nonlinear PCFs and HC PBFs; evaluate the potential use of these fibers for developing novel photonic components such as wavelength filters, super continuum sources, polarizers, polarization controllers, sensors and etc. And we discuss the splicing between PCFs and conventional single mode fibers (SMFs).

2 Single- and few-mode IG-PCFs

2.1 Single mode IG-PCF

The modal properties of an IG-PCF in many respects resemble those of a conventional step-index fiber, although the complex micro-structured cladding allows for a whole new range of novel properties. Like standard optical fibers, IG-PCF always supports at least one guided mode. The modal characteristics of an air-silica IG-PCF with a hexagonal lattice of holes are primarily determined by the air hole-diameter d and pitch Λ. Figure 3 shows the contour plot of the calculated fundamental mode field of an IG-PCF by using the finite element method (FEM) [6]. The field presents the same rotational symmetry as the PCF and the light field extends beyond the first ring of air holes.

For conventional step-index optical fibers, the V-parameter plays a central role in the description of the number of guided modes, the cutoff criterion, and the mode field diameter (MFD). An optical fiber is said to be

Received December 5, 2012; accepted December 14, 2012

E-mail: eewjin@polyu.edu.hk

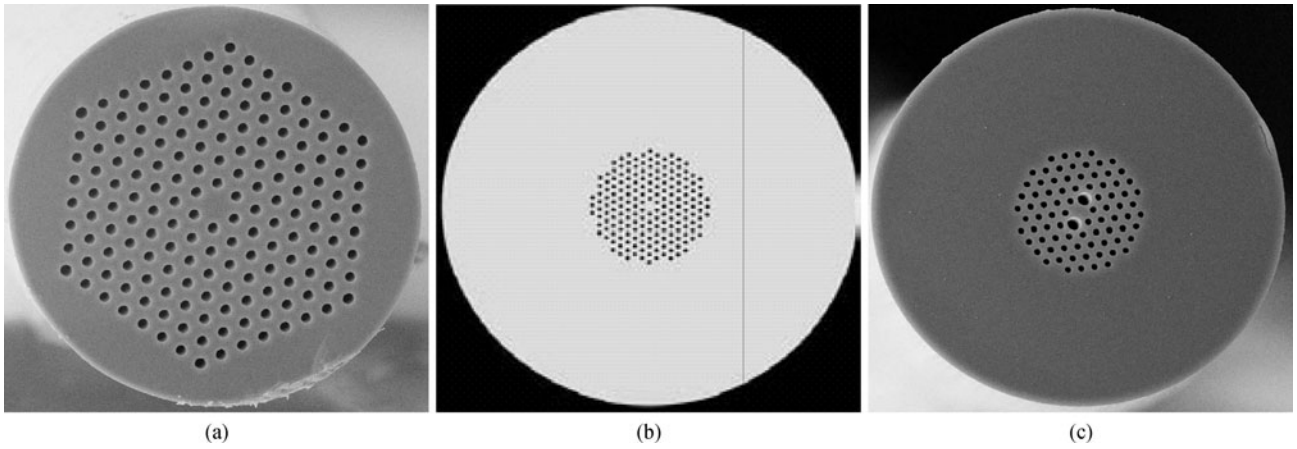

Fig. 1 Cross-sections of three types of air-silica IG-PCFs from Crystal-Fiber A/S[1)]. (a) Endlessly single mode PCF; (b) highly nonlinear PCF; (c) Hi-Bi PCF

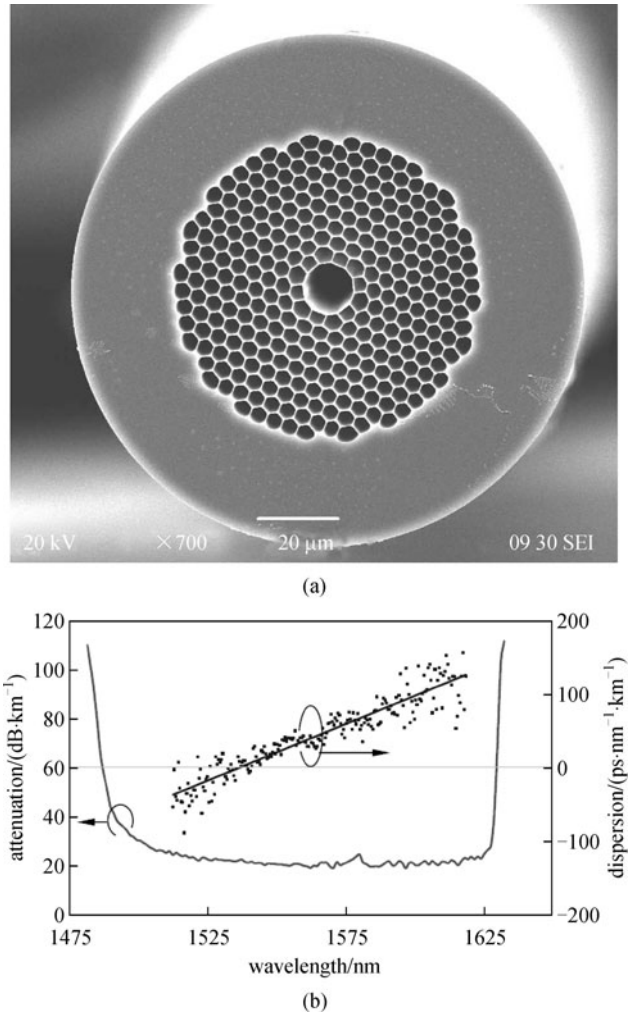

Fig. 2 (a) Scanning electron microscopy (SEM) and (b) transmission characteristics of HC PBF (HC-1550-02)[1)]. The center wavelength of this fiber is 1550 nm and the transmission window is 120 nm

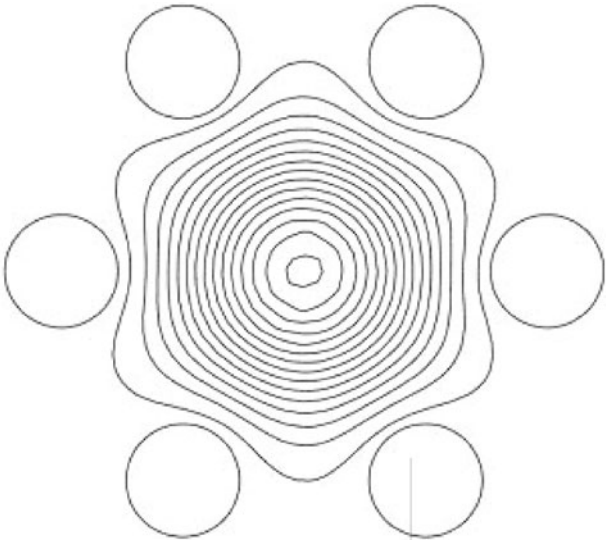

Fig. 3 Contour plot of calculated mode field for PCF with hexagonal lattice. Λ = 7.33 μm, d = 3.38 μm. The operating wavelength is 1550 nm

multimode if $V \gg 1$, where many bounded modes are supported to propagate within the core. However, when V is sufficiently small so that only the two degenerate polarization modes, i.e., the fundamental mode, can propagate, the fiber is said to be single-mode. For a standard optical fiber, it is single-mode when $V < 2.405$. In the context of PCF, the first attempt to obtain an expression for the V-parameter is based on an equivalent step-index fiber [2]. Later various definitions of V-parameter have been proposed [7,8]. For an IG-PCF with a triangular lattice of air holes, the formulation of the V-parameter is given by [8]

$$V_{\mathrm{PCF}} = \frac{2\pi}{\lambda}\Lambda\sqrt{n_{\mathrm{FM}}^2 - n_{\mathrm{FSM}}^2}, \tag{1}$$

1) http://www.nktphotonics.com/, http://www.crystal-fibre.com/

where n_{FM} and n_{FSM} are the refractive index of the fundamental mode (FM) and fundamental space-filling mode (FSM) [2], respectively. Similar to conventional fibers, the V-parameter of PCF provides plenty of information about the number of guided modes [8] and MFD [9].

It was argued in Ref. [8] that the second-order mode cutoff can be associated with $V_{PCF} = \pi$. This conclusion is indeed identical to the single-mode–multimode boundary obtained by multi-pole method [10]. Figure 4(b) shows the V_{PCF} as a function of wavelength for various values of d/Λ. With the decreasing of wavelength, the V-parameter approaches a constant value, which depends on d/Λ. The dotted line shows $V_{PCF} = \pi$ and the black dots shows the cutoff wavelength from the empirical expression [10]

$$\lambda/\Lambda \approx \alpha(d/\Lambda - 0.406)^{\gamma}, \quad (2)$$

where $\alpha = 2.80 \pm 0.12$, and $\gamma = 0.89 \pm 0.02$. As can be seen from Fig. 4, good agreement can be found between these two criteria. The phase boundary shown in Fig. 4(a) provides more direct information about the mode cutoff and was confirmed experimentally in various IG-PCFs [11].

In general, a PCF with $d/\Lambda < 0.43$ supports a single-mode and is called an endlessly SMF, and for $d/\Lambda > 0.43$ the PCF supports a second-order mode at wavelength smaller than the cutoff wavelength.

It is noticed that the core size of the PCF with a hexagonal lattice of holes is approximately 2Λ-d, and the endlessly single mode condition $d/\Lambda < 0.43$ is independent of the values of d and Λ. This indicates that single mode PCFs with large core size (or mode field area) may be made by choosing relatively large d and Λ while keeping $d/\Lambda < 0.43$. Indeed, large mode area (LMA) fibers with MFD larger than 26 μm are commercially available[1)] and these fibers may be used for applications, such as single-mode high power delivery [12], broad-band multi-wavelength transmission [1], etc.

2.2 TM IG-PCFs

Conventional step-index TM optical fibers have been investigated for a number of device applications, such as inter-modal couplers [13], selective modal filters [14], acousto-optic frequency shifters [15], dispersion compensators [16], optical switches [17], and strain and temperature sensors [18,19]. However, the wavelength range of TM operation for conventional fibers is typically less than 150 nm [20], which limit the potential applications of the TM devices. As will be shown in this section, the TM range can be expanded greatly to over one thousand nanometers, which allows the creation of extremely broadband TM fiber devices.

Considering the IG-PCF structure as shown in the inset of Fig. 5, the cut-off frequencies (wavelengths) of the guided modes may be estimated by the cross-points between their dispersion curves and that of the FSM of the cladding. Figure 5 shows the normalized cut off

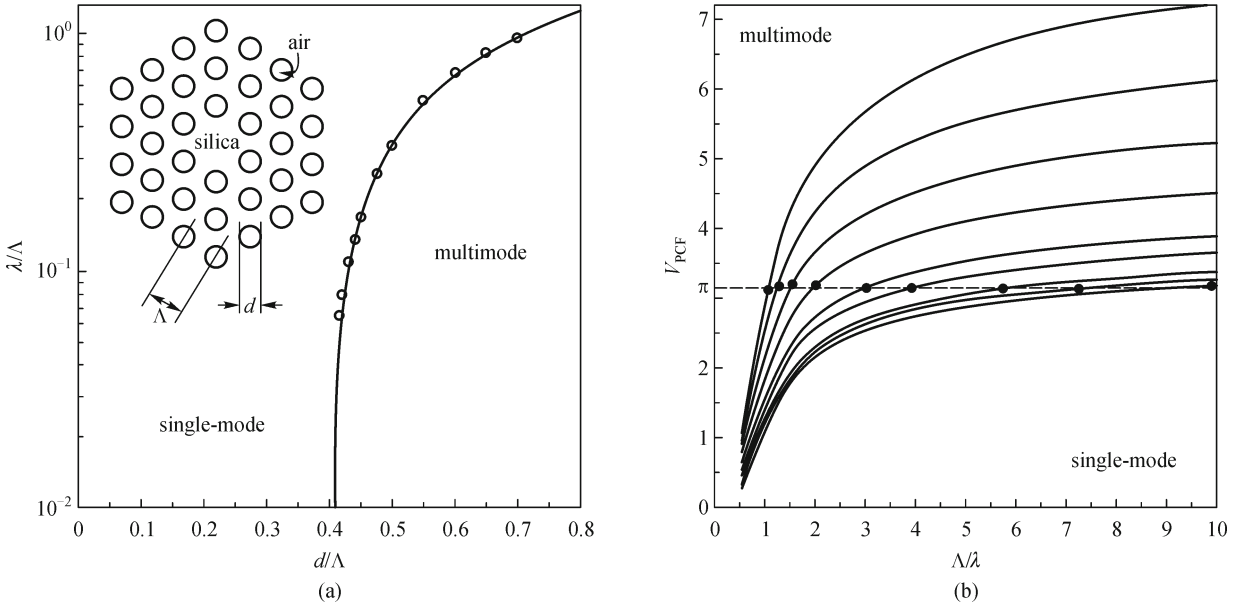

Fig. 4 (a) Single-mode–multimode phase diagram. Solid line shows phase boundary obtained by multi-pole method and circles correspond to solutions to $V_{PCF} = \pi$; (b) V_{PCF} as function of Λ/λ for $d/\Lambda = 0.43$, 0.44, 0.45, 0.475, 0.50, 0.55, 0.60, 0.65, 0.70 (from lower to upper curves). The circles correspond to the cutoff wavelength by Eq. (2) [8]

1) http://www.nktphotonics.com/, http://www.crystal-fibre.com/

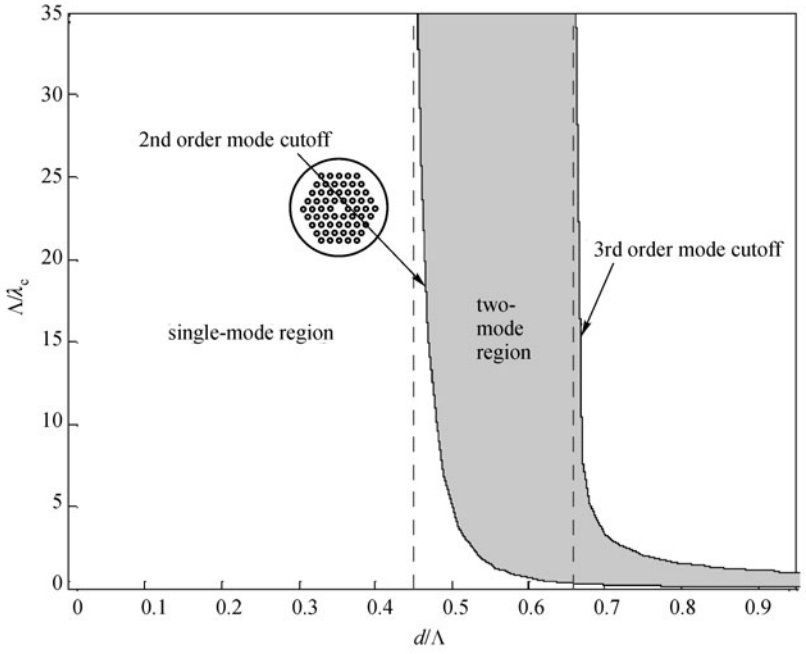

Fig. 5 Normalized cutoff wavelengths of 2nd order and 3rd order modes as functions of d/Λ [21]

frequency of the second order mode and third order modes as functions of d/Λ. Again it confirms that $d/\Lambda \approx 0.45$ bounds the endlessly single-mode region. The shaded region in Fig. 5, which corresponds approximately to d/Λ value from 0.45 to 0.65 [21], is the TM region where only the LP_{01}-like fundamental mode and the LP_{11}-like second order hybrid modes are guided. The LP_{01}-like mode includes two degenerate fundamental modes with orthogonal polarizations (HE_{11}^{x} and HE_{11}^{y}) and the LP_{11}-like mode comprises four nearly degenerate second order modes (TE_{01}, TM_{01}, and two HE_{21} modes). Take d/Λ = 0.55 as an example, the cut-off wavelength of the second order mode (LP_{01}-like mode) is 1.9 and 3.3 μm for Λ = 3 and 5 μm, which is beyond the transparent window of silica and hence the PCFs may be regarded as "endlessly TM," i.e., fibers that support two modes for any wavelength within the low loss window of silica. Figure 6 shows the mode field patterns of the first and the second order modes for a PCF with Λ = 5 μm and d/Λ = 0.6, at wavelength 1550 nm. For the same set of parameters, the beat lengths between the fundamental and the four second order modes, defined as the lengths of fiber over which the phase difference between the respective modes changes by 2π, as functions of wavelength are shown in Fig. 7. The four curves in Fig. 7 overlap, indicating the approximately degenerate nature of the four second order modes.

2.3 TM PCF acousto-optic tunable filter (AOTF)

As described in Section 2.2, the emergence of TM PCF has the potential of further enhancing the performance of the TM devices through significant expansion of the TM operating range. As an example, a novel all-fiber AOTF with an extremely large tuning range has been demonstrated [22].

The all-fiber AOTF consists of a TM PCF, an acoustic horn and a thin piezoelectric (PZT) disc attached to the horn (Fig. 8). A small hole is made at the center of the horn and the disc to allow for the unjacketed TM PCF to go through and be glued to the center of the horn. A sinusoidal electric signal excites a shear mode of the PZT vibration, of which energy is focused at the center and transferred to the fiber by the horn. The excited flexural acoustic wave traveling along the fiber results in periodic micro-bends that cause coupling between the two modes at a phase matching wavelength given by [15,22]:

$$L_B(\lambda) = \Lambda_a, \tag{3}$$

where L_B is the wavelength-dependent modal beat length; Λ_a is the acoustic wavelength of the flexural wave in PCF, which is the same as the period of the acoustically-induced micro-bends. The acousto-optic (AO) interaction takes place within length L defined from the tip of the acoustic horn to an acoustic damper, where the acoustic wave is absorbed.

When a broadband light is launched into the fundamental core-mode of the TM PCF, the phase-matched wavelength (λ) component will be coupled to the second-order LP_{11}-like core-mode, which can be removed by aligning the TM PCF precisely to the center of an output single-mode fiber or by bending the TM PCF after AO interaction. A notch-filter with a center wavelength of λ is

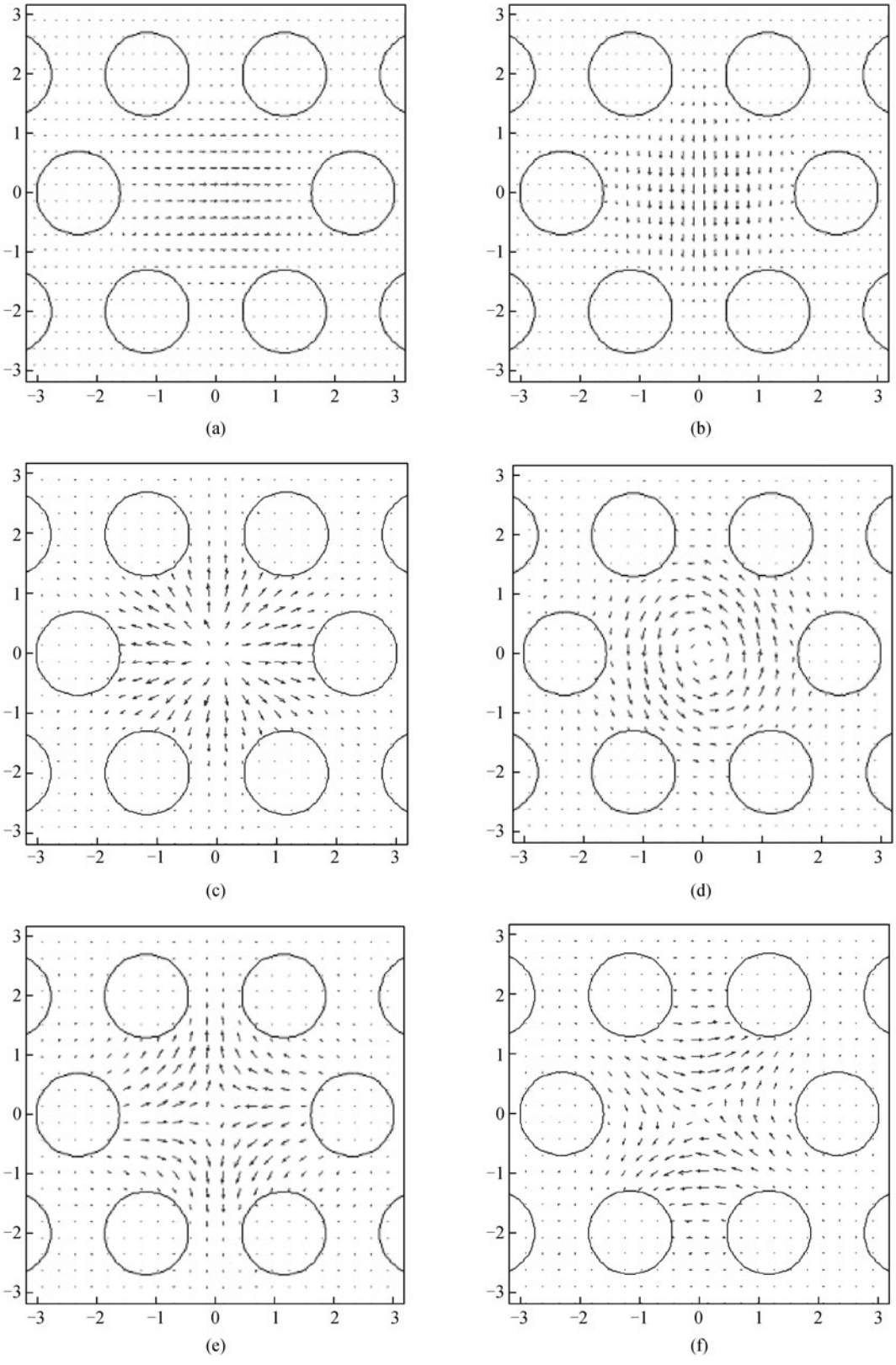

Fig. 6 Vector transverse electric field distribution of (a) HE_{11}^{x} (LP_{11}^{x}) mode; (b) HE_{11}^{y} (LP_{11}^{y}) mode; and (c) TE_{01} mode; (d) TM_{01} mode; (e) and (f) HE_{21} modes at 1550 nm. The super-position of TE_{01},TM_{01}, and HE_{21} modes gives the familiar LP_{11}-like mode patterns [21]

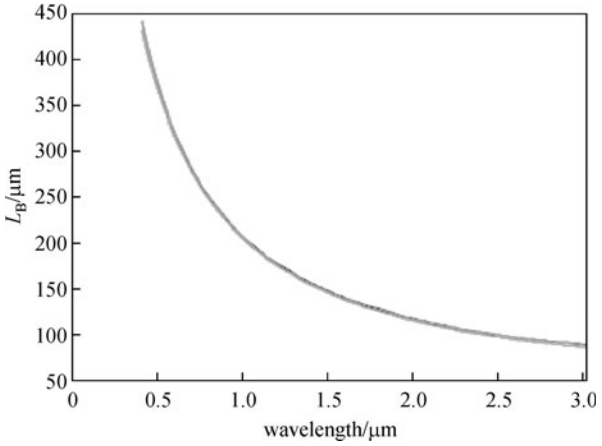

Fig. 7 Beat lengths between fundamental mode and four second-order modes as functions of wavelength [21]

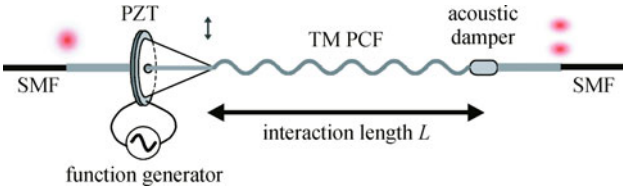

Fig. 8 AOTF based on TM PCF [22]

then realized. The important advantage of the AO device is that the center wavelength and the depth of the notch can be adjusted by tuning the frequency and the amplitude of the electrical signal applied to the PZT. The above principle has been applied to make AOTFs with conventional fibers [15,23], the dynamic range is however limited to ~200 nm due to the limited TM range and non-monotonic wavelength dependence of the modal beat length [23,24], which cause mode-coupling at multiple wavelengths and large variation of the filter linewidth dependent on the center wavelength. Such a limitation is removed by use of a TM PCF with large a TM operating wavelength range and monotonic beat-length/wavelength relationship as shown in Fig. 7.

Experimental demonstration was performed with an IG-PCF that has a similar cross-section as shown in Fig. 1(a). The average values of the relative hole-diameter (d/Λ) and the pitch (Λ) are approximately 0.49 and 9.69 μm, respectively. The AO interaction length is L = ~15.5 cm. This PCF was found to guide two core-modes for any wavelength below 2.1 μm [10,21]. They are similar to that of the LP_{01} and LP_{11} modes in conventional fibers. The modal beat-length was found to decrease monotonically from about 1800 μm at 500 nm to about 600 μm at 1700 nm and hence only one resonant wavelength is matched to a given beat length, unlike the case of conventional fibers. This feature comes from the unusually strong dispersion of the PC cladding, and results in a single-notch in the transmission spectrum of the device. There are possibilities of coupling to asymmetric cladding-modes, however, the coupling efficiencies are significantly smaller and hence we expect a single notch due to AO coupling between LP_{01}- and LP_{11}-like modes over this entire wavelength range.

The tuning characteristics of the AOTF were examined and the measured transmission spectra of the TM-PCF AOTF for various acoustic frequencies are shown in Fig. 9 (a). Only one significant resonant notch is observed in the output spectrum for each acoustic frequency, and no additional notches due to coupling to other cladding modes were observed.

Figure 9(b) shows the relationships between the center wavelength, the 3-dB linewidth of the notch and the acoustic frequency. The center wavelength was tuned from 700 to 1700 nm when the acoustic frequency was varied from 0.89 to 3.33 MHz. The experiments were limited by the spectral bandwidth of the broadband sources available

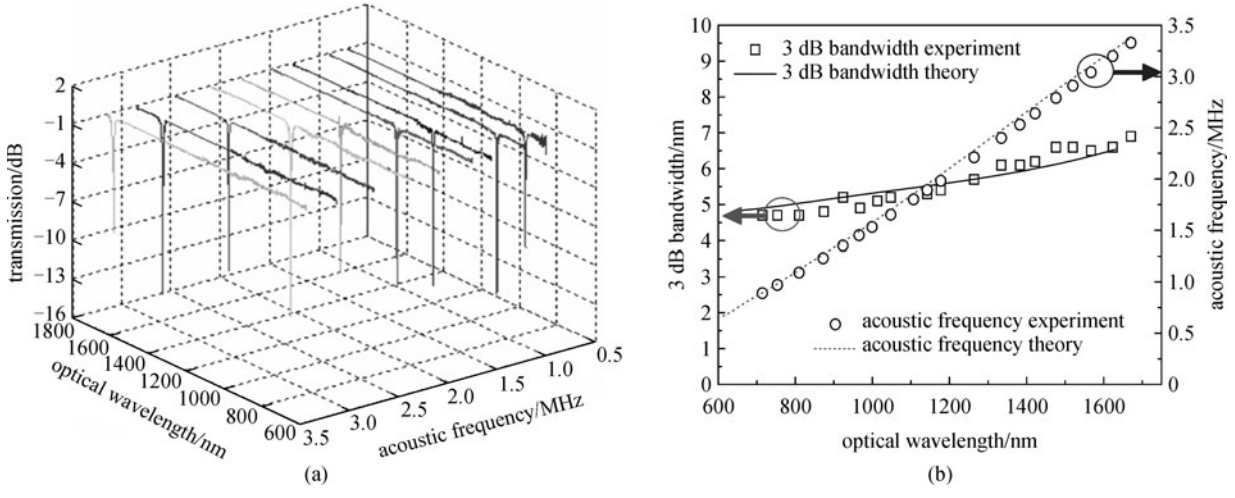

Fig. 9 Tuning characteristics of AOTF. (a) Wavelength tuning from 700 to 1700 nm; (b) relationships between center wavelength, 3-dB linewidth of notch and acoustic frequency [22]

in our laboratories. In fact, we have observed strong mode coupling at 532 and 633 nm, indicating that the dynamic range could be extended down to 532 nm and further. This suggests a possible dynamic range of over 1150 nm. The 3-dB linewidth of the resonant notch changed from 5 to 6 nm for optical wavelength from 700 to 1700 nm.

3 Hi-Bi IG-PCFs

3.1 Hi-Bi PCFs and polarizing PCFs

PCFs can be made highly birefringent by breaking its twofold symmetry. Hi-Bi PCFs can be made by having different air-hole diameters along the two orthogonal axes [5], by asymmetric core design [25,26], or by introducing stress-regions in the outer cladding surrounding the inner microstructured cladding [27]. These fibers have demonstrated modal birefringence of an order of magnitude higher than that of the conventional Hi-Bi fibers.

One of the Hi-Bi PCF structures is shown in Fig. 10. This Hi-Bi PCF is characterized by three parameters: the pitch Λ, the diameter of the small air-holes d_1, and the diameter of the two large air-holes d_2. By properly chosen values of Λ, d_1 and d_2, the PCF can be made as a polarization maintaining fiber in which both polarizations are guided with low loss [25]. It can also be made to operate in the single-polarization single-mode (SPSM) regime in which only one linear polarization is guided while the orthogonal polarization is suppressed [28,29]. The Hi-Bi PCF can also be made to guide two spatial modes (LP_{01} and LP_{11} (even)) as will be discussed in Section 3.2.

Figure 11 shows the calculated effective indices of the *x*- and *y*-polarization of the fundamental modes as functions of wavelength for a particular air-silica IG-PCF. The background refractive index was obtained from the Sellmeier equation for silica [30]. Also shown in Fig. 11 is the effective index (cladding index) of the FSM. Polarization cutoff occurs when the effective index of one of the polarization states falls below that of the FSM. As shown in Fig. 11, the cutoff wavelengths for the *x*- and *y*-polarization are respectively 1.37 and 1.62 μm, corresponding to the intersection points of their dispersion curves with that of the cladding. Single polarization operation can thus be realized within this wavelength range. For wavelength range below 1.37 μm, both polarizations are guided with low loss but the fiber is highly birefringent with index difference between the two polarizations being on the order of 10^{-3}.

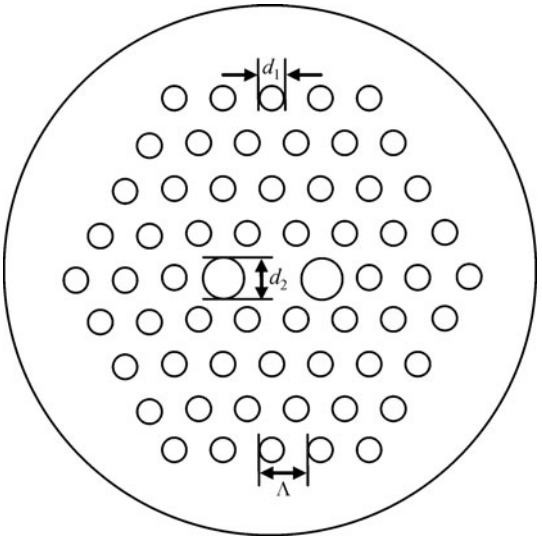

Fig. 10 Schematic cross section of Hi-Bi PCF

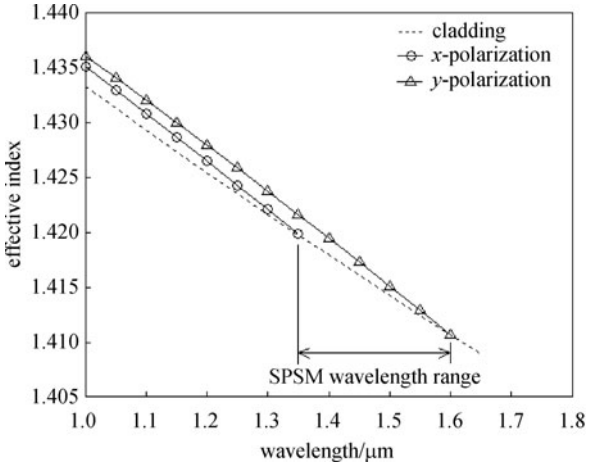

Fig. 11 Effective indices of *x*- and *y*-polarization as functions of wavelength for Hi-Bi PCF with six rings of air holes with Λ = 2.2 μm, d_1/Λ = 0.40, d_2/Λ = 0.95 [29]

The cut-off wavelengths may be designed by choosing proper values of Λ, d_1/Λ, and d_2/Λ. Numerical simulation shows that that d_1/Λ is a crucial parameter factor for the design of SPSM fibers, while d_2/Λ should be kept as high as possible [29].The cutoff wavelength as a function of Λ for different d_1/Λ is shown in Fig. 12. For smaller values of d_1/Λ, larger values of Λ can be chosen to obtain a wider single-polarization range. From Fig. 12, we note that the cutoff wavelength shows linear dependence on Λ, which is useful for SPSM PCF design. The fiber structural parameters for a desirable SPSM PCF operating at a special wavelength range can be easily obtained from Fig. 12.

Although valuable information can be extracted from the above cutoff wavelength analysis, confinement loss analysis provides practical design considerations for the leaky nature of PCF [31]. We calculated the confinement loss as function of wavelength for various PCF parameters. Figure 13 shows the calculated confinement losses to achieve SPSM operation at 1.30 and 1.55 μm wavelength bands for *x*- and *y*-polarization with eight rings of air holes. We see that low confinement losses can be obtained for

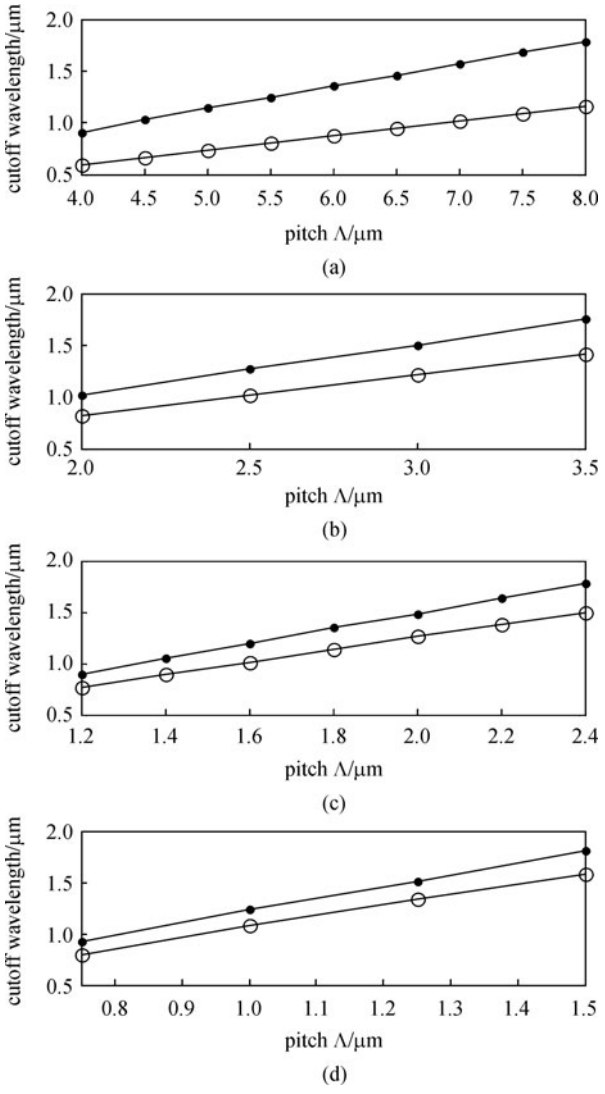

Fig. 12 Cutoff wavelength as function of pitch Λ for different ratios of d_1/Λ. Circle: *x*-polarization, dot: *y*-polarization [29]. (a) $d_1/\Lambda = 0.30$; (b) $d_1/\Lambda = 0.35$; (c) $d_1/\Lambda = 0.40$; (d) $d_1/\Lambda = 0.50$

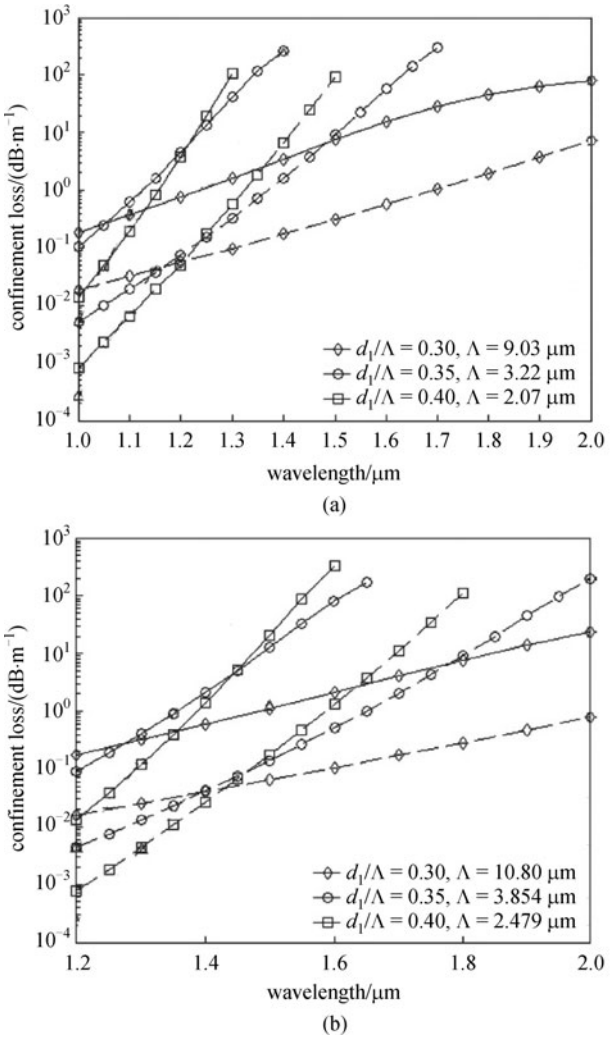

Fig. 13 Confinement loss for *x*- and *y*-polarization for SPSM PCF designed to work at (a) 1.30 μm and (b) 1.55 μm. Solid lines: *x*-polarization; dashed lines: *y*-polarization [29]

both polarization modes at wavelengths far from the cutoff values, whereas the confinement losses of *x*-polarization shows an order of magnitude higher than that of *y*-polarization.

3.2 TM Hi-Bi PCF

For the TM PCF discussed in Section 2.2, the second order LP_{11}-like mode is actually comprised of four modes (TE_{01}, TM_{01}, and HE_{21} modes) that are not perfectly degenerate, resulting in unstable lobe orientation and polarization states, especially when light travels through a longer length of fiber. In conventional step-index fiber, this problem is overcome by using an elliptical core so that the second order mode LP_{11} has a stable lobe orientation and two polarization principle axes. It is possible to introduce a high birefringence to PCF while retaining a wide TM operation range. For example, a Hi-Bi PCF with $d_1/\Lambda = 0.54$, $d_2/\Lambda = 0.98$, and $\Lambda = 6.0$ μm shows a TM range covering all the low-loss window of silica from 0.4 to 1.8 μm (Fig. 14).

There are totally four non-degenerate LP modes supported by this Hi-Bi PCF with their effective indices lies above the FSM of the cladding. The corresponding vector transverse mode field patterns are shown in Fig. 15. By analogy to the elliptical core fiber, these four modes are labeled as LP^x_{01}, LP^y_{01}, LP^x_{11} (even) and LP^y_{11} (even) mode. The superscripts *x* and *y* are corresponded respectively to the *x*- and *y*-polarization. The LP^x_{11} (odd) and LP^y_{11} (odd) modes are not supported because their index is below that of the FSM over the wavelength range from 0.4 to 1.7 μm.

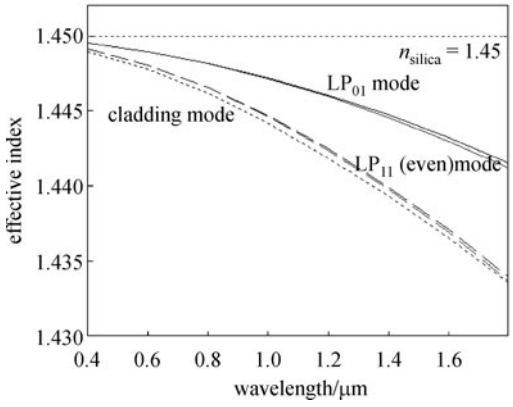

Fig. 14 Modal dispersion curve of Hi-Bi PCF. Solid lines represent the non-degenerate LP_{01} modes and dash lines represent the LP_{11} (even) modes

3.3 TM Hi-Bi PCF interferometers

The stable lobe orientations and polarization principle axes are extremely useful for TM fiber sensor applications. A TM fiber sensor uses a differential interferometric scheme, where the interference between the LP_{01} and the LP_{11} (even) modes of the fiber leads to a two-lobe pattern in the far-field of the output [20]. As has been shown in Section 3.2, a properly designed Hi-Bi PCF was found to be able to guide LP_{01} and LP_{11} (even) mode over a very broad wavelength range, over which only the two modes with a stable intensity distribution propagate along the length of the fiber [32].

Figure 16 shows the schematic plots of the far field patterns as a result of phase difference change between the LP_{01} and LP_{11} (even) modes. When the LP_{01} and LP_{11} (even) modes are excited equally in the Hi-Bi PCF, the far-field output radiation pattern will be a superposition of the contribution from the two modes and will be a function of the relative phase difference between them. The evolution of the far-field radiation for different phase difference φ results in variation in the two-lobed intensity patterns, as shown in Fig. 16. For a change in φ of 2π, there will be one complete oscillation of the intensity pattern.

An external disturbance, e.g., strain or temperature, applied on the PCF leads to a differential phase shift between these two modes, resulting in an oscillation of the two-lobe pattern. A spatial demodulator monitoring one of the two-lobe patterns at the far-field converts this oscillation into an intensity variation, from which the value of applied strain/temperature may be recovered.

The strain response of a particular Hi-Bi PCF was experimentally investigated. The cross section of the PCF is similar to that shown in Fig. 1(c) and its structural parameters are Λ = 4.179 μm, d_1 = 2.239 μm, d_2 = 4.069 μm. The length of the PCF under strain is 50 cm. Experiments were conducted at wavelength of 650, 780, 850, 980, 1300 and 1550 nm by using different semiconductor laser sources. At each wavelength, before applying axial strain to the PCF, the far field pattern at the fiber output was observed with the launching conditions varied. It is confirmed that at wavelengths from 650 to 1300 nm, this fiber supports only fundamental LP_{01} mode and LP_{11} (even) mode, and no other higher mode was observed. The intensity-lobe orientation of the LP_{11} (even) mode was found stable even when the launching condition is changed. At 1550 nm, only the LP_{01} mode can be observed, and no second order mode existed.

Measurements were performed for both the *x*- and *y*-polarization states. The strain sensitivity, defined as the rate of change of the phase difference between the two modes with respect to strain, is plotted in Fig. 17. The strain sensitivities are different for the two orthogonal polarizations but both have a linear relationship with respect to the optical wavelength. The sensitivity is higher for longer wavelength.

The response of the same Hi-Bi PCF to temperature was measured by putting a section of PCF (~1.8 m) inside an oven. The temperature sensitivity, defined as the rate of change of phase difference between the two modes with respect to temperature per unit length of sensing fiber is shown in Fig. 18. The temperature sensitivity of TM PCF is slightly different for the *x*- and *y*-polarization, and the values are in general smaller than that of the conventional elliptical core TM fibers.

The extremely broad TM wavelength range and the unusual wavelength-dependent temperature sensitivity of the TM PCF sensor provide a useful means for strain and temperature discrimination. As shown in Fig. 17, the strain sensitivities increase linearly with wavelength and are significantly different (~15%) for the two orthogonal polarizations. The temperature sensitivities have non-monotonic dependence on wavelength (Fig. 18) and are similar for both polarizations. A temperature-independent strain measurement can be readily realized by operating the interferometer at two wavelengths, where the temperature sensitivities are the same. On the other hand, it is possible to use the TM sensor for simultaneous measurement of strain and temperature by operating at two properly chosen optical wavelengths.

4 Highly nonlinear PCF

Highly nonlinear PCF is a very important category in the family of PCFs and it has a number of important applications in telecommunication, such as supercontinuum generation, wavelength conversion, fiber amplifiers, and lasers. The benefits offered by highly nonlinear PCF over conventional fiber are its enhanced nonlinearity and widely tunable and controllable dispersion properties. The nonlinear effects [34] in optical fiber are mainly attributed by the optical Kerr effect, parametric processes and inelastic scattering effects, where a number of well

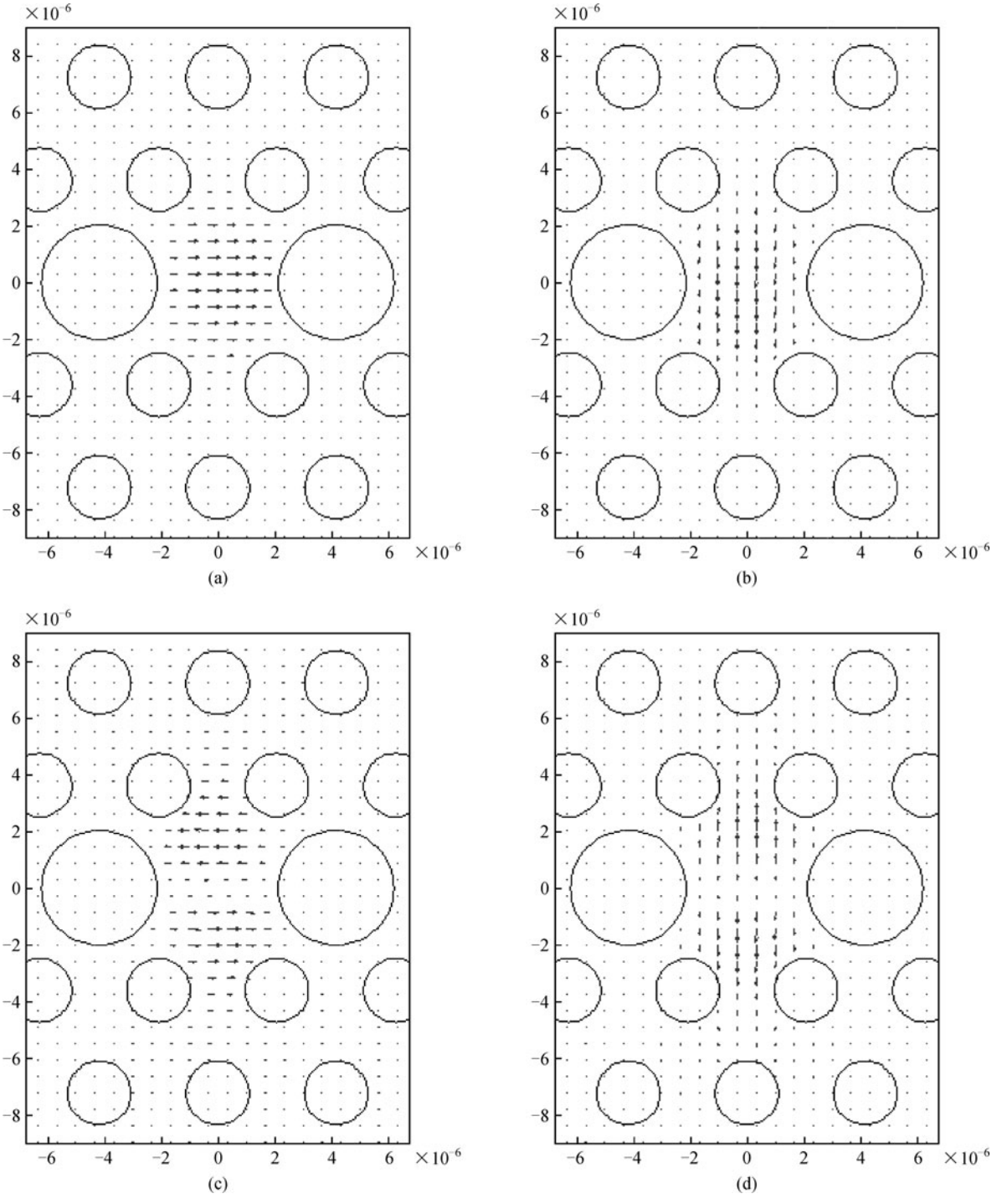

Fig. 15 Transverse electric field distribution of (a) LP_{01}^{x}; (b) LP_{01}^{y}; (c) LP_{11}^{x} (even); and (d) LP_{11}^{y} (even) modes at 1.3 μm [32]

known phenomena may be involved, such as self-phase modulation (SPM), cross-phase modulation (XPM), four-wave mixing (FWM) and stimulated Raman scattering (SRS). In general, such nonlinear effects would become obvious and utilizable only if there is strong intensity light over a long interaction length. Highly nonlinear PCF provides an excellent geometry where the light can be tightly confined in a small fiber core over a long distance. The tight confinement is achievable because the large contrast of refractive index between the core and the cladding, where a large air-filling fraction exists. The effective nonlinearity of the fiber is given by [34,35]

$$\gamma = \frac{2\pi}{\lambda}\frac{n_2}{A_{\text{eff}}}, \tag{4}$$

where n_2 is the nonlinear coefficient of the material, A_{eff} is

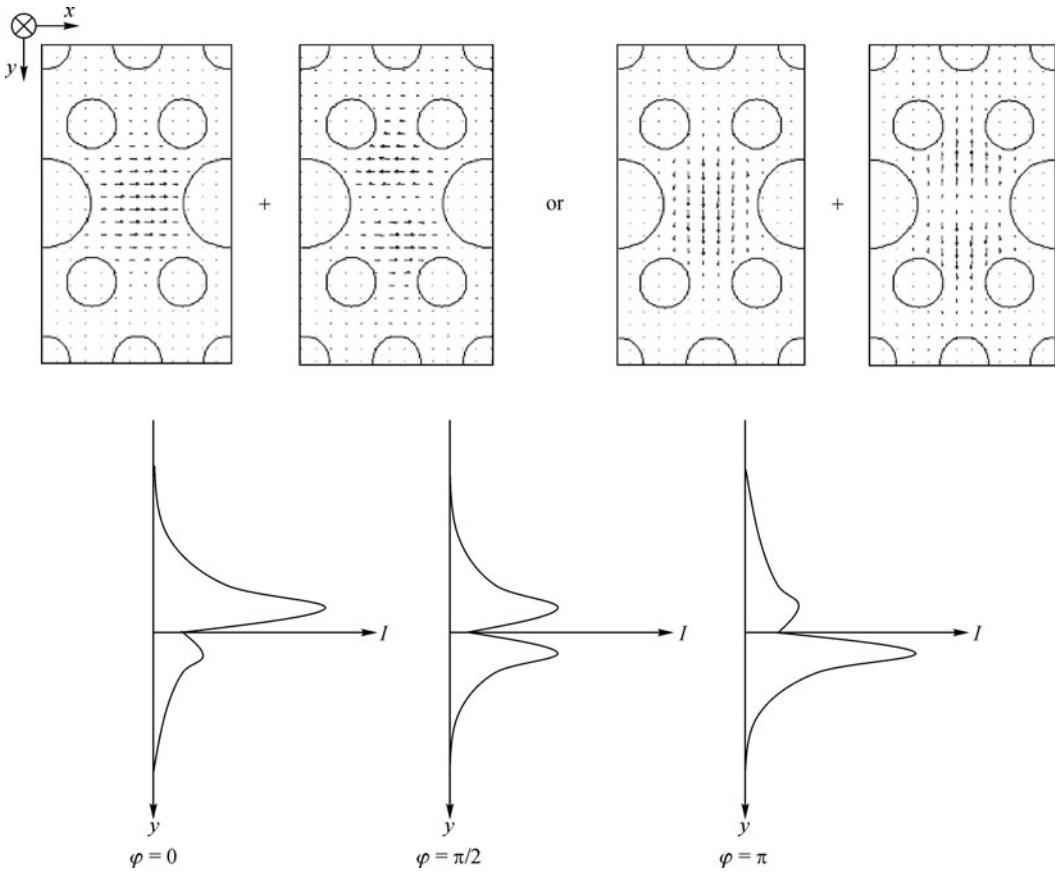

Fig. 16 Evolution of far-field patterns as function of phase difference between LP_{01} and LP_{11} (even) modes

the effective mode area, and λ is the optical wavelength. As an example, for standard SMF-28 fiber, the effective nonlinearity at 1550 nm is estimated to be about 1 $W^{-1}\cdot km^{-1}$, in which the effective mode area of the fiber and the nonlinear coefficient (n_2) of silica are approximately equal to 90 μm^2 and 2.2×10^{-20} m^2/W, respectively. In contrast, highly nonlinear PCF can achieve an effective nonlinearity as high as 52 $W^{-1}\cdot km^{-1}$ by reducing the effective mode area with a smaller core diameter (~1.7 μm) [35]. The fiber nonlinearity can be further enhanced by replacing silica glass with other glassy materials of higher nonlinear coefficient such as bismuth glass [36], lead silicate glass [37,38], tellurite glass [39], or chalcogenide glass [40].

Another important feature of PCF is its high degree of control of dispersion which can be tailored by varying the hole diameter, hole-to-hole spacing and the core diameter. PCFs have shown novel dispersion properties, such as zero-dispersion at visible or near-infrared wavelengths [41], large positive dispersion with negative dispersion slope around 1.55 μm [42] and ultra-flat dispersion over broad wavelength range [43–47].

A further important feature is that relatively large fractional power in the air-holes surrounding the core of a highly nonlinear PCF. This opens up new possibilities for exploiting the interaction of light with gases via evanescent fields in the holes [48,49]. Since PCFs can be draw into very long length and be used as a platform for light/gas (or liquid) interaction over the entire length, the PCF based evanescent wave sensors have the potential to achieve very high detection sensitivity and possibly distributed sensing along a long optical fiber.

4.1 Supercontinuum (SC) generation

SC generation is a phenomenon, in which a broadened spectrum is produced by propagation of intense optical pulses through a nonlinear media. The mechanism of SC generation is well understood which is based on a combination of nonlinear effects such as SPM, FWM and SRS [50–52]. SC generation in bulk glass requires pulses of very high peak power. In contrast, the use of optical fibers allows lower peak powers due to the long interaction length. However, the spectral broadening process is affected not only by the multitude of the nonlinear effects, but also by the dispersion properties of the fiber. In general, the widest spectra are obtained when the wavelength of the pump light is close to the zero dispersion wavelength of the fiber which restricts SC generation to the spectral region around 1.3 μm or above

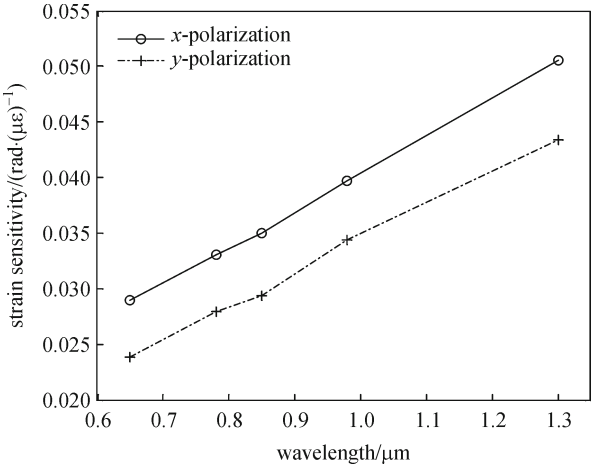

Fig. 17 Strain sensitivity as function of wavelength [32,33]

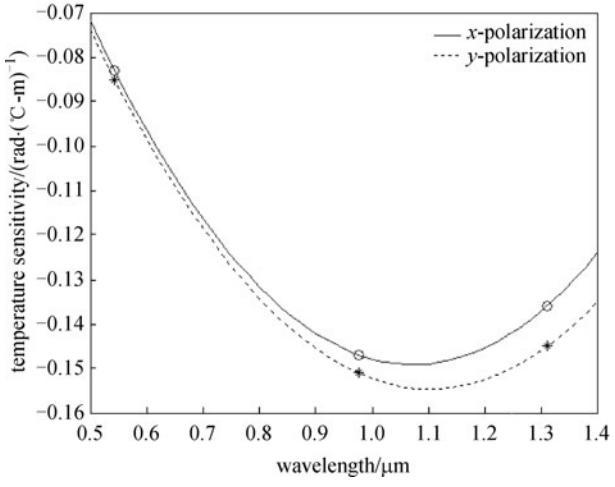

Fig. 18 Measured temperature sensitivity for *x*-polarization (circle) and *y*-polarization (star) as function of optical wavelength. Solid and dashed lines are curve fitting results of the measured data [33]

for conventional fibers. This limitation is overcome by the application of PCF in SC generation. In 2000, the PCF-based SC was first demonstrated by Ranka et al. [53] with a highly nonlinear PCF was pumped with a pulsed titanium-sapphire laser. The great advantages of highly nonlinear PCF including its enhanced effective nonlinearity and designable dispersion properties were clearly shown. Afterward, substantial amount of research on SC generation with highly nonlinear PCFs has been reported [54–61]. With rapid development, SC has been generated not only with pulsed laser operating in femtosecond but all regimes including continuous wave (CW) [62,63].

As an example, Fig. 19 shows the SC spectrum generated from the 75-cm long highly nonlinear PCF

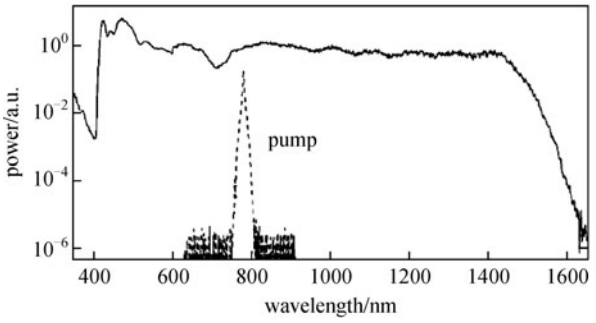

Fig. 19 SC spectrum reported by Ranka et al. [53] in 2000

with a 1.7 μm core diameter and anomalous dispersion at 800 nm [53]. The pump source used was a pulsed titanium-sapphire laser operating at 790 nm. The pulse duration and energy of the pump laser are 100 fs and 800 pJ, respectively.

In fact, SC sources employing highly nonlinear PCF are commercially available. A series of SC sources covering wavelength range from 460 to 2400 nm is released by Koheras[1]. The output power of such white light sources is as high as few watts. SC sources have many applications [64]. For example, they have been used in a variety of nonlinear spectroscopy [65,66], optical coherence tomography [67] and optical frequency metrology [68,69]. They have also been used in the dense wavelength division multiplexing (DWDM), in which the SC is spectrally sliced to create multi-wavelength source [70,71].

4.2 Evanescent wave gas sensor

The evanescent field in the air holes is absorbed by gas species [72,73], and the gas concentration can be obtained from the intensity attenuation through the Beer-Lambert law

$$I(\lambda) = I_{\mathrm{o}}(\lambda)\exp\left(-r\alpha_{\mathrm{m}}(\lambda)lC\right), \tag{5}$$

where I and I_{o} are respectively the output light intensities with and without the presence of the gas being detected. $\alpha_{\mathrm{m}}(\lambda)$ is the absorption coefficient of the gas being measured and is a function of wavelength. l is the length of the PCF used for gas detection (interaction length) and C is the gas concentration. r is a relative sensitivity coefficient defined as [73]

$$r = (n_{\mathrm{r}}/n_{\mathrm{e}})f, \tag{6}$$

where n_{r} is the index of the gas species and is approximately equal to 1. n_{e} is the effective index of the guided mode. f is the fraction of the total power located in the holes.

The relative sensitivity r is affected by a number of

1) http://www.koheras.com/

parameters including operating wavelength λ, the core-size, the size of the air-holes d and the pitch Λ in the cladding. PCFs designed for nonlinear applications typically have significant evanescent power in the cladding holes and hence are suitable candidates for absorption based gas sensors.

For the PCF shown in Fig. 20, the relative sensitivity coefficient as a function of wavelength is calculated by using FEM and shown in Fig. 21. At wavelengths of 1.53 and 1.65 μm, corresponding to absorption lines of Acetylene (C_2H_2) and Methane (CH_4) gases, the relative sensitivities are respectively ~13% and ~15% that of an open path cell per equal length. This sensitivity is over 50 times larger than the D-shaped optical fiber [74]. Theoretical simulation shows that the relative sensitivity increases with the operating wavelength λ and relative hole size d/Λ, but decreases with structural size d or Λ (for the same d/Λ). There have been reported that highly nonlinear PCF with very small core and large air-holes can achieve a relative sensitivity as large as 30% [49,75].

The highly nonlinear PCF may be used as a platform for gas analysis in laboratory, in which very long interaction length and small hole-sizes would allow for very high sensitivity gas concentration measurement while consuming only minute volume of sample gas. For such an application, the response time is not much of a concern because the sample can be pumped into the hole-columns through pressure differential.

For field applications where pressure differential is not guaranteed, the long response time due to time taken for gas to diffuse into the holes needs to be considered. As size of the holes in the PCF is small, the wall effect between the molecules and the wall of the hole-column may need to be

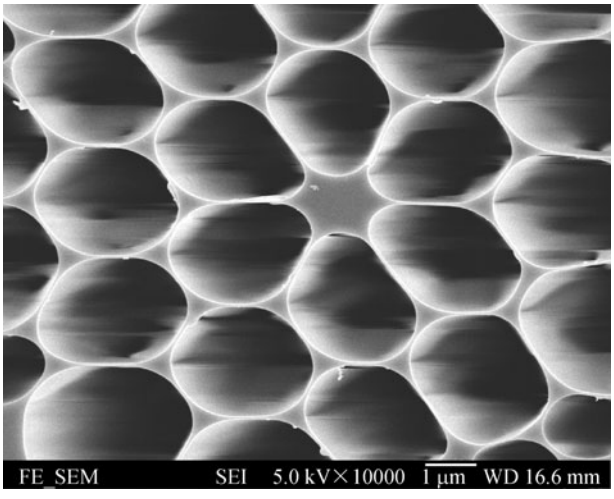

Fig. 20 SEM photo of cross-section of highly nonlinear fiber from Crystal- Fiber A/S[1]. Diameter of the central silica region is 1.7 μm. $\Lambda = 3.24$ μm and $d = 3$ μm

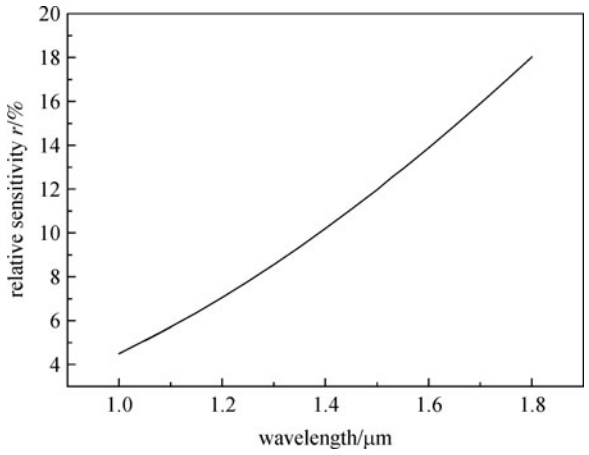

Fig. 21 Relative sensitivity of Crystal Fiber's PCF as function of wavelength [49]

taken into account. The Knudsen number ($K_n = m/d$) is usually used to represent the wall effect of a capillary diffusion system [76], where m is the mean free path of the gas molecules and d is the diameter of the capillary tube (the hole diameter here). If the Knudsen number is small, diffusion has the same characteristics as in the continuum state. If the Knudsen number is larger than one, diffusion will be dominated by the wall effect. A study of the diffusion of acetylene gas into the air-holes for the PCF shown in Fig. 20 was carried out by using the both-ends-open-for-diffusion model as shown in Fig. 22; and the results show that, because of the very small Knudsen number of acetylene and air, the diffusion process is close to the continuum state and the wall effect only reduces the diffusion coefficient by a small factor ($< 9\%$). The response time, defined as the time taken for the average acetylene concentration in the air-columns over the entire sensing length reaches 90% C_0 (the externally applied acetylene concentration) is found to be 12, 33, 63, and 478 s for 3, 5, 7 and 20 cm lengths of fiber.

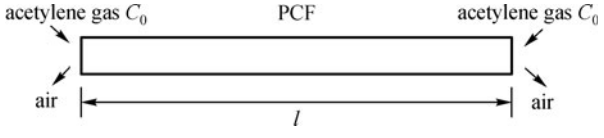

Fig. 22 Model for studying dynamics of gas diffusion into holes of PCF

For gas sensing application that requires response time of ~1 min, the length of the sensing PCF should be limited to less than 7 cm, assuming both ends are open for diffusion. The sensitivity of the sensor is then limited because of the short sensing fiber length allowed. To achieve higher sensitivity with reasonable response time, one may use a longer length of sensing fiber and introduce

1) http://www.nktphotonics.com/, http://www.crystal-fibre.com/

periodic side openings along sensing fiber to allow faster diffusion of gas into the evanescent wave region. This design would improve sensitivity without comprising response time.

5 HC PBFs

As have been discussed in Section 1, the periodic air-hole array in the cladding has PBGs that allow the guiding of light in a hollow-core. HC PBFs allow the confinement of an optical mode and gas/liquid phase materials simultaneously within the hollow-core. This provides an excellent platform for strong light/gas interaction inside the fiber-core over a very long distance, and is beneficial to a number of applications in spectroscopy, frequency metrology, nonlinear optics, sensors and instrumentation.

Since the first air/silica HC PBFs were demonstrated in 1999 [3], significant progress has been made in the design and fabrication of these fibers. The minimum fiber loss has been reduced down to 13 dB/km in 2003 [77] and 1.2 dB/km in 2005 [78]. HC PBFs with transmission bands centered at different wavelengths from 450 to 1.55 μm are commercially available[1)]. HC PBFs with core sizes from 5 to 50 μm, formed by removing different number of unit cells in a triangular array of air-holes, are experimentally demonstrated [79]. These fibers support a single, a few or many transverse modes within the PBG of the cladding. The HC PBF can also be made highly birefringent to reduce polarization mode coupling and to realize polarization maintaining transmission [80]. The HC PBFs, although are not yet as superior as the state of the art conventional silica TIR fibers in terms of transmission loss, they are however sufficient for many applications that requires relatively shorter length of fibers.

5.1 Gas-filled HC PBFs

One of the most successful applications of the HC PBF technology is the novel gas cells based on such fibers. A gas cell can be made by splicing two ends of a gas-filled HC PBF to two pieces of conventional SMFs. The gas-filling may also be carried after splicing by utilizing side-holes drilled along the HC PBF [81–83]. The gas pressure inside the hollow core may be varied from below 0.01 mbar to up to atmospheric pressure. Many applications have been demonstrated with such gas cells or gas filled fibers, including high sensitivity spectroscopic detection of acetylene [84], methane [85] and ammonia gases [86], stimulated Raman scattering in hydrogen [87], laser wavelength stabilization with acetylene gas cells [81], saturated absorption in acetylene and hydrogen cyanide [88], electromagnetically-induced transparency in acetylene [89], etc. Benabid et al. [87] demonstrated Raman wavelength conversion in a hydrogen-filled hollow-core fiber and achieved Stokes generation with threshold energy of only 800 nJ and anti-Stokes generation of 3.4 μJ, which are two orders of magnitudes lower than previous results.

5.2 Liquid-filled HC PBFs

The hollow-core and/or the air holes in the cladding can be selectively filled with liquid or polymeric materials to create fibers with novel sensing properties. By filling the core and the cladding holes simultaneously by a fluid with an refractive index higher than silica, or selectively filling the core by a fluid will transform a HC PBF to an IG-TIR fiber with which intensity (e.g., absorption), phase (frequency) and polarization modulation sensors; and Raman sensors may be implemented [90–93].

Filling the core and cladding holes simultaneously by a liquid with an index lower than silica maintains the PBG guidance but the bandgaps and hence the transmission bands shift with the index of the filling material [94]. This is a novel sensing mechanism that does not exist in IG-TIR fibers. In addition to bandgap position, dispersion within the bandgap also varies with refractive index of the filling material. Figure 23 shows the theoretically calculated transmission bands when the holes in a commercial HC PBF (HC-1550-02) are filled with various refractive index liquids. Figure 24 shows the measured transmission characteristics when the hollow-core and cladding holes are filled liquids with indexes of 1.30, 1.33 and 1.36, respectively.

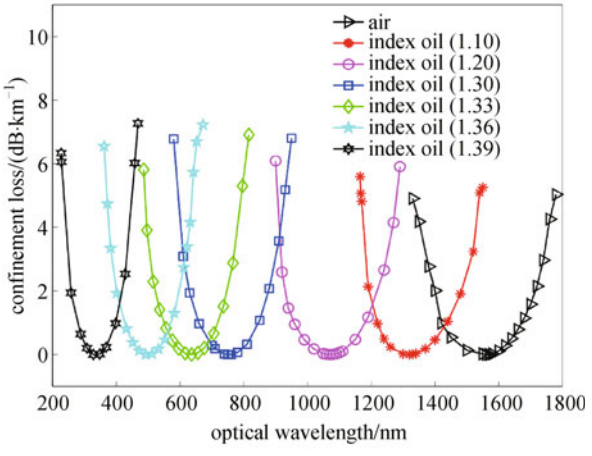

Fig. 23 Calculated transmission bands when holes in HC-1550-02 PBF[1)] are filled with various refractive index liquids [94]

By selectively filling the hollow-core and/or cladding holes with different refractive index polymer or liquid, hybrid fibers which guide light simultaneously by IG- and PBG-guiding or by two overlapping sets of PBGs,

1) http://www.nktphotonics.com/, http://www.crystal-fibre.com/

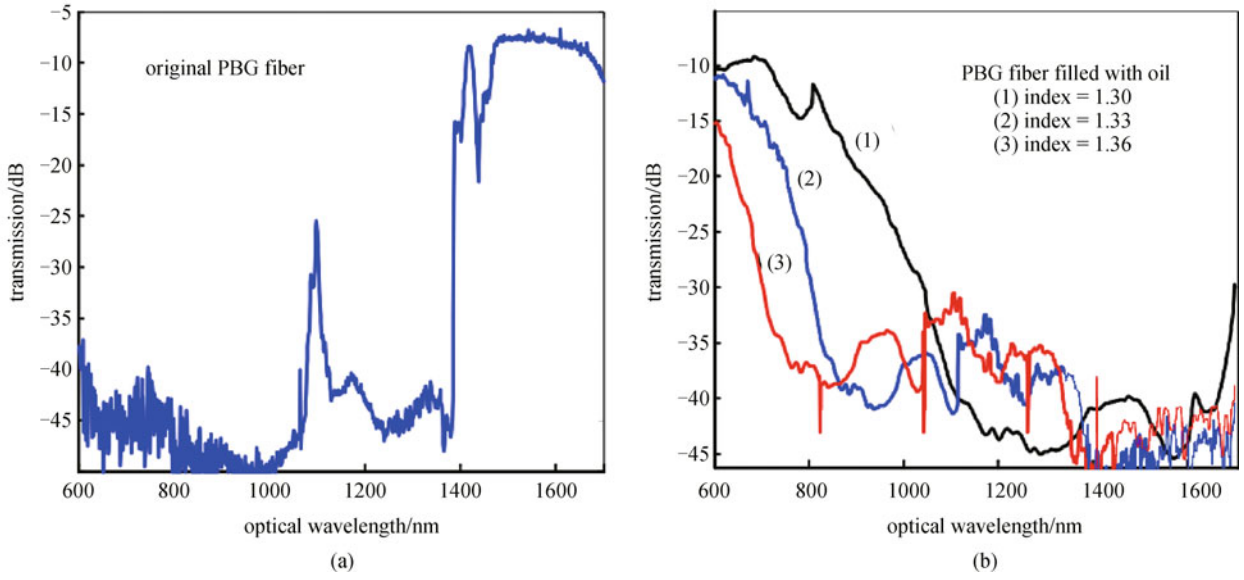

Fig. 24 Transmission characteristics of HC-1550-02 fiber when hollow-core and cladding holes are filled with materials of different refractive indexes [94]

corresponding to two parts of cladding with different refractive index contrasts, may be created. This technique may be employed to create fibers with adjustable bandgap and dispersions [95]. The properties of these hybrid fibers are sensitive to bend, as well as temperature if materials with different thermal coefficients are used to fill the holes [96,97].

5.3 HC PBF components

To fully realize the potential of HC PBFs, they need to be integrated with other components and devices to form systems or sub-systems. One way to achieve this is to splice HC PBG functional fibers to conventional fiber systems, which will be discussed in Section 7.

Sometimes, there is an advantage to form all HC PBF systems and this needs to develop components based on HC PBFs. Terrel et al. [98] demonstrated a polarization controller consisting of three twistable sections of HC-1550-02 fiber and achieved a bandwidth of 13 nm. We built a polarization controller by pressurizing laterally three segments of HC-PBF (Fig. 25); by varying the magnitudes of the applied pressures, a good coverage of all the possible polarization states on the Poincare sphere was achieved [99]. Ozcan et al. [100] investigated the properties of tapered HC-1550-2 fibers and found that the fiber is highly sensitive to tapering and the weak tapers may be used an in-line filters of high resolution.

We have successfully made long period gratings (LPGs) by use of a CO_2 laser to periodically collapse some of the air-holes along one side of a HC PBF [101]. These LPGs couple the fundamental air-core mode into higher order core modes [102] and have unique properties such as in-

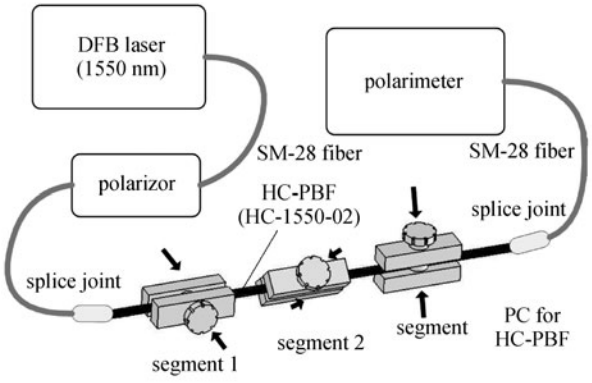

Fig. 25 HC-PBF polarization controller [99]

sensitivity to bend and low sensitivity to temperature. By using a similar method, we have made a HC-PBF polarizer as shown in Fig. 26 [103]. The partial collapse of air-holes on one side of the fiber results in an asymmetric waveguide structure, in which one polarization leaks out while the orthogonal polarization remains propagating along the fiber with relatively low-loss. These polarizers have extinction ratios from 20 to beyond 30 dB over a wavelength range from 50 to 110 nm (Fig. 27).

6 HC PBF sensors

One of the potential applications of HC-PBF is highly sensitive and distributed gas detection. Compared with the nonlinear PCF discussed in Section 4.2, HC PBFs can achieve a higher detection sensitivity with a shorter length

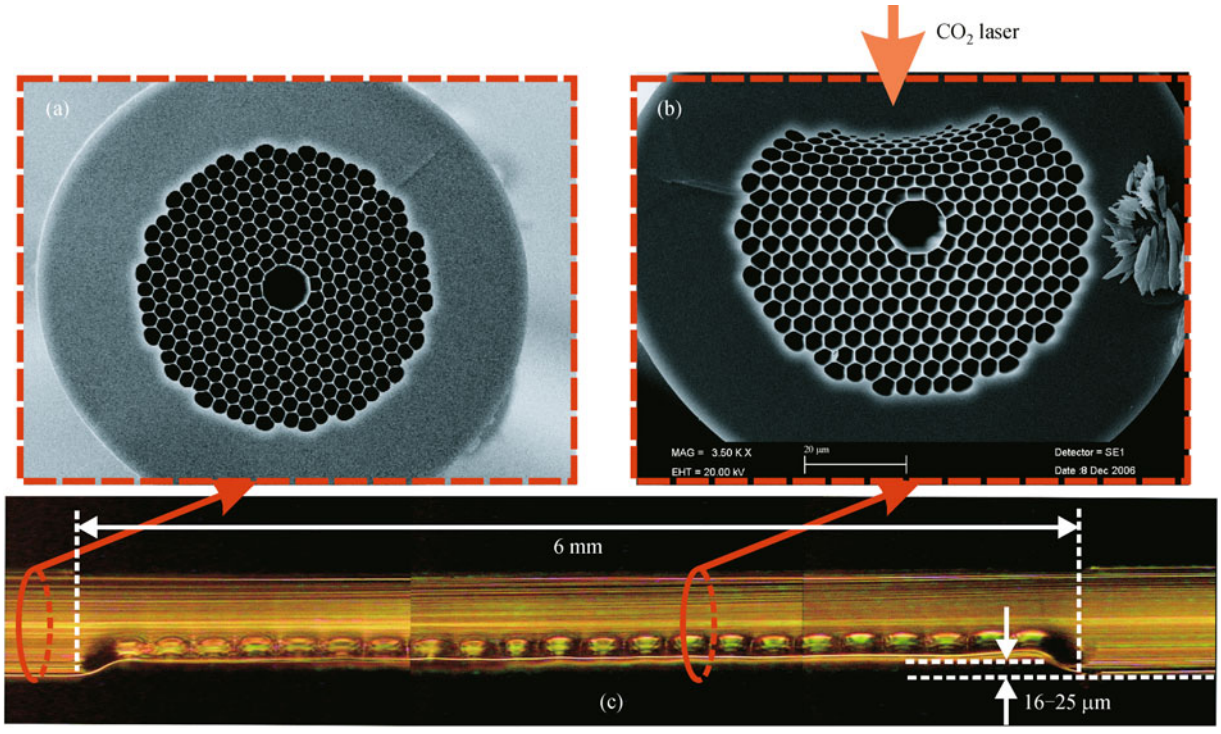

Fig. 26 (a) SEM image of original HC-1550-02 PBF; (b) cross-section and (c) side view of valley created by CO_2 laser irradiation. Only segments of the valley are shown in (c) [103]

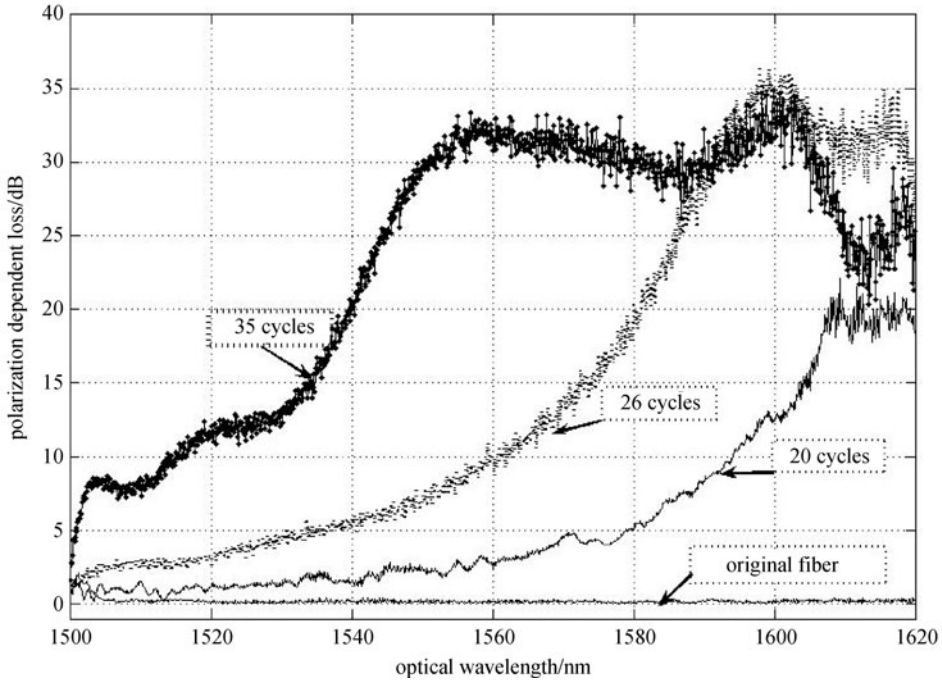

Fig. 27 Evolution of polarization extinction ratio of HC-PBF polarizer for increasing degree of air-hole collapse in the cladding, corresponding to increasing number of scanning cycles [103]

of fiber because of the much larger percentage of light power (>95%) interacting with the gas sample. We were the first group that demonstrated the absorption-based gas detection in HC-PBF [104]. Recently, we demonstrated the

drilling of micro-channels (Fig. 28) from the side of HC-PBFs by use of a femtosecond infrared laser. The side-channels introduce very little loss and an average loss of ~0.05 dB per channel around 1550 nm has been achieved. The side-channels speed up the gas in/out diffusion process, and make it possible to use a long sensing length to achieve higher sensitivity but maintain a reasonably fast response [105].

The acoustic sensitivity of the HC PBF can be made significantly higher than a standard SMF. The phase sensitivity of a fiber mode to acoustic pressure is determined by the pressure-induced changes in the fiber length and in the effective refractive index. By reducing the area of silica in the fiber cross-section, the effective Young's modulus of the HC PBF can be made significantly smaller than a solid fiber and hence the induced change in the fiber length could be much bigger. In addition, in a standard solid fiber, the pressure-induced index change is significant and has opposite sign with respect to the length change, which comprises the acoustic sensitivity. In a HC-PBF, most of the fundamental mode power travel in air instead of silica, the index change is then much less affected by acoustic pressure. Our theoretical modeling showed that, by using a thin outer silica cladding of the order of a few micrometers and an air-filling ratio of 95% or higher, the acoustic sensitivity of a HC PBF can be made − 35 dB higher than a standard silica fiber [106]. A further 20 dB improvement could be achieved by optimizing the thickness of the outer polymer jacket.

7 Splicing PCFs with SMFs

To realize the full potential of PCFs, it is necessary to couple light efficiently between conventional SMFs and PCFs. Low-loss splicing of PCFs with SMFs would allow the incorporation of PCFs into conventional optical fiber systems and hence enable more widespread applications of PCFs. The splice loss between PCFs and SMFs may be considered to be mainly due to two reasons: the mode field mismatch between the two types of fibers and the induced collapse of air-holes of PCFs in the vicinity of splice-joints during the splicing process. The collapse of air-holes may significantly increase the coupling loss by destroying the light guiding structure of the PCF near the splice joint.

Detailed investigations on splicing various commercial PCFs (Table 1) with SMF-28 fibers by using an Ericsson FSU-975 fusion splicer have been carried out [107,108]. It was found that different splicing methods or conditions are required to achieve low-loss splicing between SMFs and different PCFs. A precise alignment and a proper selection of the fusion parameters (including fusion current and duration, overlap, offset, and the number of repeated discharges) are the key to achieve optimal splicing. For PCFs (e.g., LMA10 PCF and PM-1550-01) that have similar MFDs to that of SMFs, low-loss splicing may be achieved by minimizing the collapse of air holes in the PCF by using a proper offset and low current and short duration arc discharges (Fig. 29(b)). For PCFs and SMFs with significant MFD mismatch, minimization of air-hole collapse may not guarantee low loss splicing. For PCFs (e.g., LMA5 PCF, or NL-1550-POS-1) with low to medium air-filling fraction and MFDs smaller than that of the SMF, low-loss splicing may be achieved by applying repeated low-level arc discharges over the splicing joint to gradually collapse the air holes of the PCFs; the repeated discharges partially collapse the holes and reduce the air-filling fraction and hence enlarge the MFD (Fig. 29(d)). Figure 30 shows the cross-section of LMA5 PCF after different number of repeated discharges. The hole-size reduces significantly after a large number of discharges (Fig. 30(b)), which raises the average refractive index of the cladding and expands the mode field into the cladding region. For small-core PCFs with very high air-filling

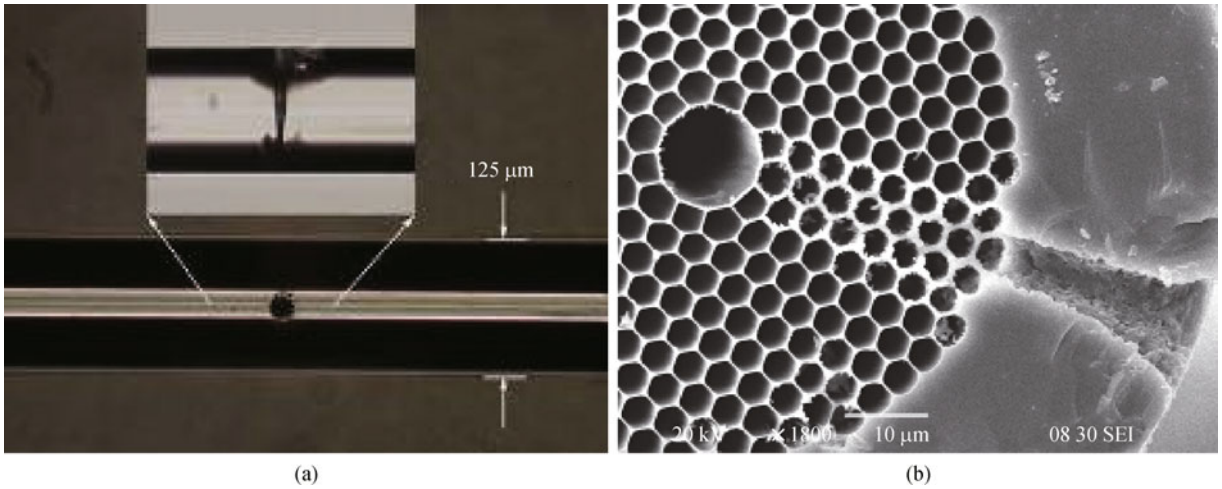

Fig. 28 Micro-channel drilled into core of HC-PBF, allowing faster response for gas detection. (a) Side view; (b) cross-section

Table 1 Different PCFs and fiber parameter at 1550 nm[1)] [107]

fiber	core diameter/μm	relative hole size d/Λ	pitch Λ /μm	MFD/μm	numerical aperture/NA
LMA-10	10.71	0.46	7.14	8.5	0.14
HC-1550-02	10.9	> 90%*	3.8	7.5	0.12
LMA-5	4.5	0.44	2.9	4.1	0.23
NL-3.3-880	3.4	>89%*	3.0	2.2	0.41
PM-1550-01	—	large hole 0.97 small hole 0.51	4.17	long axis 3.6 short axis 3.1	—
SMF-28	8.3	—	—	10.4	0.14

Note: * Air filling fraction

fraction (e.g., NL-3.3-800 PCF), partial collapse of the cladding holes may not help, and an intermediate fiber (e.g., UHNA3 from Nufern) with a small MFD similar to that of the PCF in one end and with MFD enlarged to match the SMF on the other end may be used to reduce the splice loss (Fig. 29(c)). In splicing SMFs to HC PBFs, it was noticed that, in addition to the partial collapse of air holes, a recess at the end of the HC PBF [81] was created due to surface tension. This creates an air-gap between the two fibers and would increase the coupling loss. We have demonstrated low-loss splicing of different PCFs with conventional SMFs, and the optimized splice results are listed in Table 2. It should be mentioned that the measured loss for the SMF28/HC-1550-02 splice is from SMF to HC PBF, the loss from HC PBF to SMF is considerably larger (>2.5 dB), because higher order modes may be excited in HC-1550-02 and they are not coupled well into the SMF. The results may be further improved by using a fusion splicer which has a higher precision in alignment and in controlling fusion energy. The experimental results confirm that fusion splicing is a simple but still practical solution to solve the coupling problem between PCFs and SMFs, which will benefit the development of different PCF devices and sensors in practical applications.

8 Summary

This paper reviews some of the recent developments in PCFs, devices and sensors. The coverage is not exhaustive but rather discusses some of the work we are familiar with. Significant part of the work described here was actually carried out in the laboratories of ourselves and our collaborators. The research on PCF is continuing and it is expected that many new developments and applications will come out in the near future. One particular interesting area of development may be the development of components and systems based on HC-PBFs. The novel light guiding mechanisms and properties of the HC-PBFs will allow the development of novel devices, and sensors

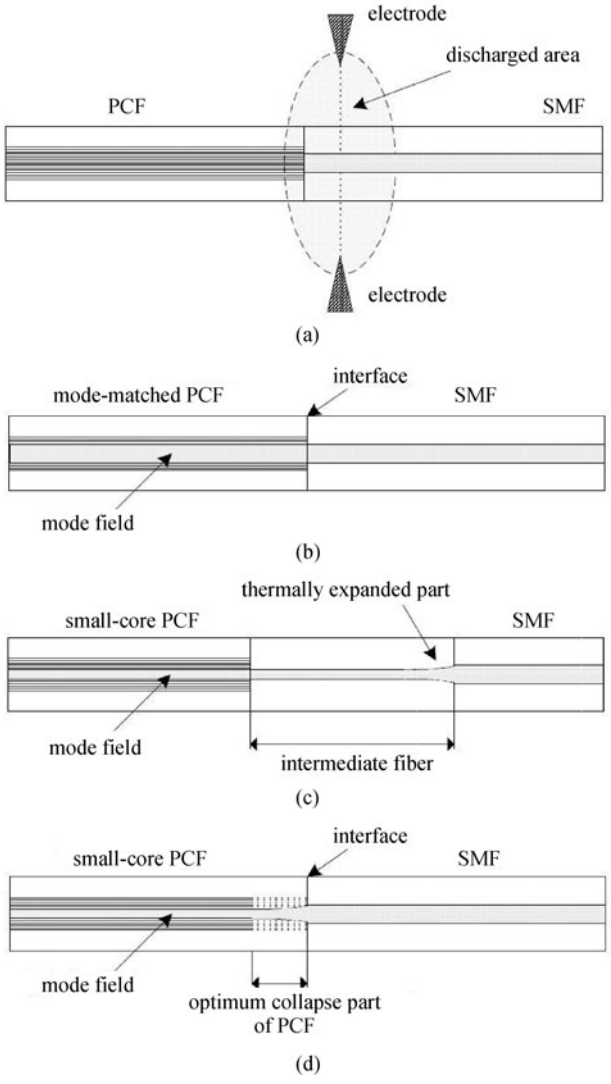

Fig. 29 (a) Splicing SMF to PCF with offset of the joint to the central axis of arc discharge; (b) splicing SMF to PCF having the same MFD; (c) splicing SMF to small-core PCF with an intermediate fiber; (d) splicing SMF to small-core PCF with a controlled collapse of air-holes to enlarge the model field [107]

1) http://www.nktphotonics.com/, http://www.crystal-fibre.com/

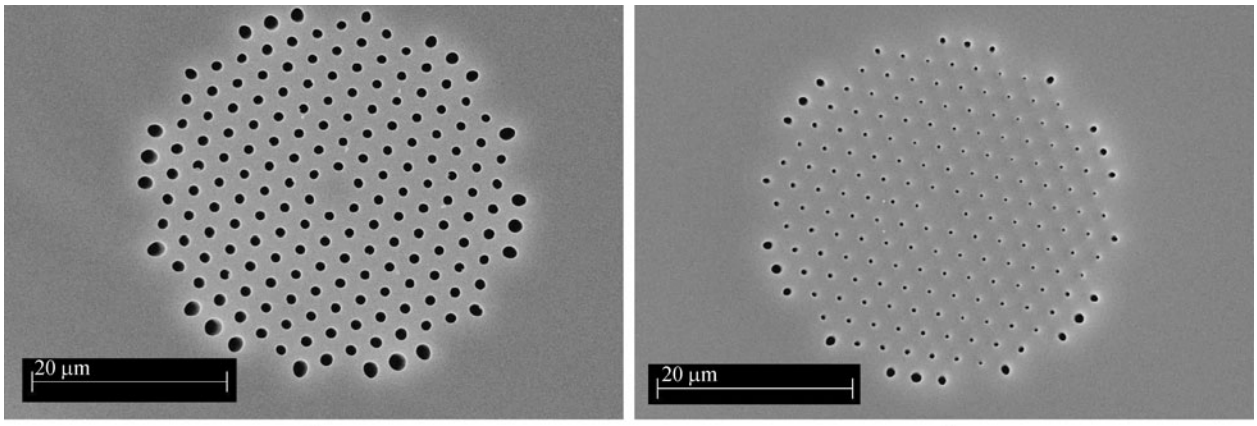

Fig. 30 End views of LMA-5 after (a) two and (b) seven discharges. The fusion duration, fusion current, and offset are respectively 0.3 s, 10 mA and 50 μm [107]

Table 2 Splice losses from SMF28 to different PCFs [107]

splice type	theoretical coupling loss/dB	butt-coupling loss/dB	optimized splice loss/dB
SMF-28/LMA-10	0.18	0.41	0.19
SMF-28/HC-1550-02	0.46	1.50	1.45
SMF-28/LMA-5	3.32	3.62	0.90
SMF-28/NL-3.3-880	7.85	8.14	2.53
SMF-28/PM-1550-01	4.70	4.88	2.03

with superior performance over their conventional fiber counterparts.

Acknowledgements The research work was partially supported by the Hong Kong SAR government (Nos. PolyU5196/09E, PolyU5182/07E, PolyU5187/06E); the National Natural Science Foundation of China (Grants Nos. 61290313 and 60629401), the Hong Kong Polytechnic University (No. J-BB9K). We thank Y. P. Wang, H. F. Xuan, L. M. Xiao, K. S. Hung, H. C. Park, D. N. Wang, M. Zhang, C. L. Zhao, Y. B. Liao, I. K. Hwang, Z. Wang, M. S. Demokan, H. Y. Tam, B. Y. Kim and R. S. Windeler for their contributions/inputs at different stages of the research.

References

1. Knight J C, Birks T A, Russell P St J, Atkin D M. All-silica single-mode optical fiber with photonic crystal cladding. Optics Letters, 1996, 21(19): 1547–1549
2. Birks T A, Knight J C, Russell P S. Endlessly single-mode photonic crystal fiber. Optics Letters, 1997, 22(13): 961–963
3. Cregan R F, Mangan B J, Knight J C, Birks T A, Russell P S, Roberts P J, Allan D C. Single-mode photonic band gap guidance of light in air. Science, 1999, 285(5433): 1537–1539
4. Broderick N G R, Monro T M, Bennett P J, Richardson D J. Nonlinearity in holey optical fibers: measurement and future opportunities. Optics Letters, 1999, 24(20): 1395–1397
5. Ortigosa-Blanch A, Knight J C, Wadsworth W J, Arriaga J, Mangan B J, Birks T A, Russell P, St J. Highly birefringent photonic crystal fibers. Optics Letters, 2000, 25(18): 1325–1327
6. Ju J, Jin W, Demokan M S. Properties of a highly birefringent photonic crystal fiber. IEEE Photonics Technology Letters, 2003, 15(10): 1375–1377
7. Knight J, Birks T, Russell P, de Sandro J. Properties of photonic crystal fiber and the effective index model. Journal of the Optical Society of America. A, Optics, Image Science, and Vision, 1998, 15(3): 748
8. Mortensen N A, Folkenberg J R, Nielsen M D, Hansen K P. Modal cutoff and the V parameter in photonic crystal fibers. Optics Letters, 2003, 28(20): 1879–1881
9. Nielsen M D, Mortensen N A, Folkenberg J R, Bjarklev A. Mode-field radius of photonic crystal fibers expressed by the V parameter. Optics Letters, 2003, 28(23): 2309–2311
10. Kuhlmey B T, McPhedran R C, Martijn de Sterke C. Modal cutoff in microstructured optical fibers. Optics Letters, 2002, 27(19): 1684–1686
11. Folkenberg J R, Mortensen N A, Hansen K P, Hansen T P, Simonsen H R, Jakobsen C. Experimental investigation of cutoff phenomena in nonlinear photonic crystal fibers. Optics Letters, 2003, 28(20): 1882–1884
12. Limpert J, Schreiber T, Nolte S, Zellmer H, Tunnermann T, Iliew R, Lederer F, Broeng J, Vienne G, Petersson A, Jakobsen C. High-power air-clad large-mode-area photonic crystal fiber laser. Optics Express, 2003, 11(7): 818–823

13. Blake J N, Kim B Y, Shaw H J. Fiber-optic modal coupler using periodic microbending. Optics Letters, 1986, 11(3): 177
14. Sorin W V, Kim B Y, Shaw H J. Highly selective evanescent modal filter for two-mode optical fibers. Optics Letters, 1986, 11 (9): 581–583
15. Kim B Y, Blake J N, Engan H E, Shaw H J. All-fiber acousto-optic frequency shifter. Optics Letters, 1986, 11(6): 389–391
16. Poole C D, Wiesenfeld J M, McCormick A R, Nelson K T. Broadband dispersion compensation by using the higher-order spatial mode in a two-mode fiber. Optics Letters, 1992, 17(14): 985–987
17. Park H S, Song K Y, Yun S H, Kim B Y. All-fiber wavelength-tunable acoustooptic switches based on intermodal coupling in fibers. Journal of Lightwave Technology, 2002, 20(10): 1864–1868
18. Murphy K A, Miller M S, Vengsarkar A M, Claus R O. Elliptical-core two mode optical-fiber sensor implementation methods. Journal of Lightwave Technology, 1990, 8(11): 1688–1696
19. Vengsarkar A M, Michie W C, Jankovic L, Culshaw B, Claus R O. Fiber-optic dual-technique sensor for simultaneous measurement of strain and temperature. Journal of Lightwave Technology, 1994, 12(1): 170–177
20. Kim B Y, Blake J N, Huang S Y, Shaw H J. Use of highly elliptical core fibers for two-mode fiber devices. Optics Letters, 1987, 12(9): 729–731
21. Jin W, Wang Z, Ju J. Two-mode photonic crystal fibers. Optics Express, 2005, 13(6): 2082–2088
22. Hong K S, Park H C, Kim B Y, Hwang I K, Jin W, Ju J, Yeom D I. 1000 nm tunable acousto-optic filter based on photonic crystal fiber. Applied Physics Letters, 2008, 92(3): 031110
23. Engan H E, Kim B Y, Blake J N, Shaw H J. Propagation and optical interaction of guided acoustic waves in two-mode optical fibers. Journal of Lightwave Technology, 1988, 6(3): 428–436
24. Yun S H, Hwang I K, Kim B Y. All-fiber tunable filter and laser based on two-mode fiber. Optics Letters, 1996, 21(1): 27–29
25. Suzuki K, Kubota H, Kawanishi S, Tanaka M, Fujita M. Optical properties of a low-loss polarization-maintaining photonic crystal fiber. Optics Express, 2001, 9(13): 676–680
26. Hansen T P, Broeng J, Libori S E B, Knudsen E, Bjarklev A, Jensen J R, Simonsen H. Highly birefringent index-guiding photonic crystal fibers. IEEE Photonics Technology Letters, 2001, 13(6): 588–590
27. Folkenberg J, Nielsen M, Mortensen N, Jakobsen C, Simonsen H. Polarization maintaining large mode area photonic crystal fiber. Optics Express, 2004, 12(5): 956–960
28. Kubota H, Kawanishi S, Koyanagi S, Tanaka M, Yamaguchi S. Absolutely single polarization photonic crystal fiber. IEEE Photonics Technology Letters, 2004, 16(1): 182–184
29. Ju J, Jin W, Demokan M S. Design of single-polarization single-mode photonic crystal fiber at 1.30 and 1.55 μm. Journal of Lightwave Technology, 2006, 24(2): 825–830
30. Marcuse D. Light Transmission Optics. New York: Van Nostrand Reinhold, 1982
31. White T P, McPhedran R C, de Sterke C M, Botten L C, Steel M J. Confinement losses in microstructured optical fibers. Optics Letters, 2001, 26(21): 1660–1662
32. Ju J, Jin W, Demokan M S. Two-mode operation in highly birefringent photonic crystal fiber. IEEE Photonics Technology Letters, 2004, 16(11): 2472–2474
33. Ju J, Wang Z, Jin W, Demokan M S. Temperature sensitivity of a two-mode photonic crystal fiber interferometric sensor. IEEE Photonics Technology Letters, 2006, 18(20): 2168–2170
34. Agrawal G P. Nonlinear Fiber Optics. New York: Academic Presss, 2007
35. Finazzi V, Monro T M, Richardson D J. Small-core silica holey fibers: nonlinearity and confinement loss trade-offs. Journal of the Optical Society of America. B, Optical Physics, 2003, 20(7): 1427
36. Ebendorff-Heidepriem H, Petropoulos P, Asimakis S, Finazzi V, Moore R C, Frampton K, Koizumi F, Richardson D, Monro T M. Bismuth glass holey fibers with high nonlinearity. Optics Express, 2004, 12(21): 5082–5087
37. Kiang K M, Frampton K, Monro T M, Moore R, Tucknott J, Hewak D W, Richardson D J, Rutt H N. Extruded singlemode non-silica glass holey optical fibres. Electronics Letters, 2002, 38(12): 546
38. Kumar V V R, George A K, Reeves W H, Knight J C, Russell P St J, Omenetto F G, Taylor A J. Extruded soft glass photonic crystal fiber for ultrabroad supercontinuum generation. Optics Express, 2002, 10(25): 1520–1525
39. Kumar V V R, George A K, Knight J C, Russell P St J. Tellurite photonic crystal fiber. Optics Express, 2003, 11(20): 2641–2645
40. Monro T M, West Y D, Hewak D W, Broderick N G R, Richardson D J. Chalcogenide holey fibres. Electronics Letters, 2000, 36(24): 1998
41. Ferrando A, Silvestre E, Andres P, Miret J J, Andres M V. Designing the properties of dispersion-flattened photonic crystal fibers. Optics Express, 2001, 9(13): 687–697
42. Reeves W H, Knight J C, Russell P St J, Roberts P J. Demonstration of ultra-flattened dispersion in photonic crystal fibers. Optics Express, 2002, 10(14): 609–613
43. Saitoh K, Koshiba M, Hasegawa T, Sasaoka E. Chromatic dispersion control in photonic crystal fibers: application to ultra-flattened dispersion. Optics Express, 2003, 11(8): 843–852
44. Hansen K P. Dispersion flattened hybrid-core nonlinear photonic crystal fiber. Optics Express, 2003, 11(13): 1503–1509
45. Renversez G, Kuhlmey B, McPhedran R. Dispersion management with microstructured optical fibers: ultraflattened chromatic dispersion with low losses. Optics Letters, 2003, 28(12): 989–991
46. Shen L P, Huang W P, Jian S S. Design of photonic crystal fibers for dispersion-related applications. Journal of Lightwave Technology, 2003, 21(7): 1644–1651
47. Hoo Y L, Jin W, Ju J, Ho H L, Wang D N. Design of photonic crystal fibers with ultra-low, ultra-flattened chromatic dispersion. Optics Communications, 2004, 242(4–6): 327–332
48. Hoo Y L, Jin W, Ho H L, Wang D N, Windeler R S. Evanescent-wave gas sensing using microstructure fiber. Optical Engineering (Redondo Beach, Calif.), 2002, 41(1): 8–9
49. Hoo Y L, Jin W, Shi C Z, Ho H L, Wang D N, Ruan S C. Design and modeling of a photonic crystal fiber gas sensor. Applied Optics, 2003, 42(18): 3509–3515
50. Stolen R H, Lee C, Jain R K. Development of the stimulated Raman spectrum in single-mode silica fibers. Journal of the Optical

Society of America. B, Optical Physics, 1984, 1(4): 652
51. Baldeck P L, Alfano R R. Intensity effects on the stimulated four photon spectra generated by picosecond pulses in optical fibers. Journal of Lightwave Technology, 1987, 5(12): 1712–1715
52. Ilev I, Kumagai H, Toyoda K, Koprinkov I. Highly efficient wideband continuum generation in a single-mode optical fiber by powerful broadband laser pumping. Applied Optics, 1996, 35(15): 2548–2553
53. Ranka J K, Windeler R S, Stentz A J. Visible continuum generation in air-silica microstructure optical fibers with anomalous dispersion at 800 nm. Optics Letters, 2000, 25(1): 25–27
54. Coen S, Chau A H C, Leonhardt R, Harvey J D, Knight J C, Wadsworth W J, Russell P, St J. White-light supercontinuum generation with 60-ps pump pulses in a photonic crystal fiber. Optics Letters, 2001, 26(17): 1356–1358
55. Coen S, Chau A H L, Leonhardt R, Harvey J D, Knight J C, Wadsworth W J, Russell P, St J. Supercontinuum generation by stimulated Raman scattering and parametric four-wave mixing in photonic crystal fibers. Journal of the Optical Society of America. B, Optical Physics, 2002, 19(4): 753–764
56. Dudley J M, Provino L, Grossard N, Maillotte H, Windeler R S, Eggleton B J, Coen S. Supercontinuum generation in air–silica microstructured fibers with nanosecond and femtosecond pulse pumping. Journal of the Optical Society of America. B, Optical Physics, 2002, 19(4): 765–771
57. Gaeta A L. Nonlinear propagation and continuum generation in microstructured optical fibers. Optics Letters, 2002, 27(11): 924–926
58. Yamamoto T, Kubota H, Kawanishi S, Tanaka M, Yamaguchi S. Supercontinuum generation at 1.55 m in a dispersion-flattened polarization-maintaining photonic crystal fiber. Optics Express, 2003, 11(13): 1537–1540
59. Hundertmark H, Kracht D, Wandt D, Fallnich C, Kumar V V R K, George A K, Knight J C, Russell P St J. Supercontinuum generation with 200 pJ laser pulses in an extruded SF6 fiber at 1560 nm. Optics Express, 2003, 11(24): 3196–3201
60. Prabhu M, Taniguchi A, Hirose S, Lu J, Musha M, Shirakawa A, Ueda K. Supercontinuum generation using Raman fiber laser. Applied Physics. B, Lasers and Optics, 2003, 77(2–3): 205–210
61. Abeeluck A K, Headley C, Jørgensen C G. High-power supercontinuum generation in highly nonlinear, dispersion-shifted fibers by use of a continuous-wave Raman fiber laser. Optics Letters, 2004, 29(18): 2163–2165
62. Avdokhin A V, Popov S V, Taylor J R. Continuous-wave, high-power, Raman continuum generation in holey fibers. Optics Letters, 2003, 28(15): 1353–1355
63. Abeeluck A K, Headley C. Continuous-wave pumping in the anomalous- and normal-dispersion regimes of nonlinear fibers for supercontinuum generation. Optics Letters, 2005, 30(1): 61–63
64. Agrawal G P. Application of Nonlinear Fiber Optics, New York: Academic Press, 2008
65. Kano H, Hamaguchi H. Dispersion-compensated supercontinuum generation for ultrabroadband multiplex coherent anti-Stokes Raman scattering spectroscopy. Journal of Raman Spectroscopy, 2006, 37(1–3): 411–415
66. Nagahara T, Imura K, Okamoto H. Time-resolved scanning near-field optical microscopy with supercontinuum light pulses generated in microstructure fiber. Review of Scientific Instruments, 2004, 75(11): 4528
67. Hartl I, Li X D, Chudoba C, Ghanta R K, Ko T H, Fujimoto J G, Ranka J K, Windeler R S. Ultrahigh-resolution optical coherence tomography using continuum generation in an air-silica microstructure optical fiber. Optics Letters, 2001, 26(9): 608–610
68. Diddams S A, Jones D J, Ye J, Cundiff S T, Hall J L, Ranka J K, Windeler R S, Holzwarth R, Udem T, Hansch T W. Direct link between microwave and optical frequencies with a 300 THz femtosecond laser comb. Physical Review Letters, 2000, 84(22): 5102–5105
69. Holzwarth R, Udem T, Hansch T W, Knight J C, Wadsworth W J, Russell P St J. Optical frequency synthesizer for precision spectroscopy. Physical Review Letters, 2000, 85(11): 2264–2267
70. Takara H, Ohara T, Sato K. Over 1000 km DWDM transmission with supercontinuum multi-carrier source. Electronics Letters, 2003, 39(14): 1078
71. Yusoff Z, Petropoulos P, Furusawa K, Monro T M, Richardson D J. A 36-channel × 10-GHz spectrally sliced pulse source based on supercontinuum generation in normally dispersive highly nonlinear holey fiber. IEEE Photonics Technology Letters, 2003, 15 (12): 1689–1691
72. Monro T M, Richardson D J, Bennett P J. Developing holey fibres for evanescent field devices. Electronics Letters, 1999, 35(14): 1188
73. Stewart G, Norris J, Clark D F, Culshaw B. Evanescent-wave chemical sensors–a theoretical evaluation. International Journal of Optoelectronics, 1991, 6(3): 227–238
74. Stewart G, Jin W, Culshaw B. Prospects for fibre-optic evanescent-field gas sensors using absorption in the near-infrared. Sensors and Actuators. B, Chemical, 1997, 38(1–3): 42–47
75. Ho H L, Hoo Y L, Jin W, Ju J, Wang D N, Windeler R S, Li Q. Optimizing microstructured optical fibers for evanescent wave gas sensing. Sensors and Actuators. B, Chemical, 2007, 122(1): 289–294
76. Cussler E L. Diffusion: Mass Transfer in Fluid Systems. New York: Cambridge University, 1997
77. Smith C M, Venkataraman N, Gallagher M T, Müller D, West J A, Borrelli N F, Allan D C, Koch K W. Low-loss hollow-core silica/air photonic bandgap fibre. Nature, 2003, 424(6949): 657–659
78. Roberts P J, Couny F, Sabert H, Mangan B J, Williams D P, Farr L, Mason M W, Tomlinson A, Birks T A, Knight J C, St J, Russell P. Ultimate low loss of hollow-core photonic crystal fibres. Optics Express, 2005, 13(1): 236–244
79. Amezcua-Correa R, Broderick N G R, Petrovich M N, Poletti F, Richardson D J. Design of 7 and 19 cells core air-guiding photonic crystal fibers for low-loss, wide bandwidth and dispersion controlled operation. Optics Express, 2007, 15(26): 17577–17586
80. Chen X, Li M J, Venkataraman N, Gallagher M T, Wood W A, Crowley A M, Carberry J P, Zenteno L A, Koch K W. Highly birefringent hollow-core photonic bandgap fiber. Optics Express, 2004, 12(16): 3888–3893
81. Benabid F, Couny F, Knight J C, Birks T A, Russell P St J. Compact, stable and efficient all-fibre gas cells using hollow-core

photonic crystal fibres. Nature, 2005, 434(7032): 488–491
82. Thapa R, Knabe K, Corwin K L, Washburn B R. Arc fusion splicing of hollow-core photonic bandgap fibers for gas-filled fiber cells. Optics Express, 2006, 14(21): 9576–9583
83. Hensley C J, Broaddus D H, Schaffer C B, Gaeta A L. Photonic band-gap fiber gas cell fabricated using femtosecond micromachining. Optics Express, 2007, 15(11): 6690–6695
84. Hoo Y L, Jin W, Ho H L, Ju J, Wang D N. Gas diffusion measurement using hollow-core photonic bandgap fiber. Sensors and Actuators. B, Chemical, 2005, 105(2): 183–186
85. Kornaszewski L W, Gayraud N, Stone J M, Macpherson W N, George A K, Knight J C, Hand D P, Reid D T. Mid-infrared methane detection in a photonic bandgap fiber using a broadband optical parametric oscillator. Optics Express, 2007, 15(18): 11219–11224
86. Cubillas A M, Hald J, Petersen J C. High resolution spectroscopy of ammonia in a hollow-core fiber. Optics Express, 2008, 16(6): 3976–3985
87. Benabid F, Knight J C, Antonopoulos G, Russell P, St J. Stimulated Raman scattering in hydrogen-filled hollow-core photonic crystal fiber. Science, 2002, 298(5592): 399–402
88. Henningsen J, Hald J, Peterson J C. Saturated absorption in acetylene and hydrogen cyanide in hollow-core photonic bandgap fibers. Optics Express, 2005, 13(26): 10475–10482
89. Benabid F, Light P S, Couny F, Russell P, St J. Electromagnetically-induced transparency grid in acetylene-filled hollow-core PCF. Optics Express, 2005, 13(15): 5694–5703
90. Fini J M. Microstructure fibres for optical sensing in gases and liquids. Measurement Science & Technology, 2004, 15(6): 1120–1128
91. De Matos C J S, Cordeiro C M B, Dos Santos E M, Ong J S K, Bozolan A, Brito Cruz C H. Liquid-core, liquid-cladding photonic crystal fibers. Optics Express, 2007, 15(18): 11207–11212
92. Xiao L, Jin W, Demokan M S, Ho H L, Hoo Y L, Zhao C. Fabrication of selective injection microstructured optical fibers with a conventional fusion splicer. Optics Express, 2005, 13(22): 9014–9022
93. Han Y, Oo M K K, Zhu Y N, Xiao L M, Demohan M S, Jin W, Du H. Index-guiding liquid-core photonic crystal fiber for solution measurement using normal and surface-enhanced Raman scattering. Optical Engineering (Redondo Beach, Calif.), 2008, 47(4): 040502
94. Xuan H F, Jin W, Ju J, Ho H L, Zhang M, Liao Y B. Low-contrast photonic bandgap fibers and their potential applications in liquid-base sensors. In: Proceedings of the Society for Photo-Instrumentation Engineers, 2007, 6619: 36
95. Xiao L M, Jin W, Demokan M S. Photonic crystal fibers confining light by both index-guiding and bandgap-guiding: hybrid PCFs. Optics Express, 2007, 15(24): 15637–15647
96. Wang Y P, Tan X L, Jin W, Liu S J, Ying D Q, Hoo Y L. Improved bending property of half-filled photonic crystal fiber. Optics Express, 2010, 18(12): 12197–12202
97. Wang Y P, Tan X L, Jin W, Ying D Q, Hoo Y L, Liu S J. Temperature-controlled transformation in fiber types of fluid-filled photonic crystal fibers and applications. Optics Letters, 2010, 35 (1): 88–90
98. Terrel M, Digonnet M J F, Fan S. Polarization controller for hollow-core fiber. Optics Letters, 2007, 32(11): 1524–1526
99. Pang M, Jin W. A hollow-core photonic bandgap fiber polarization controller. Optics Letters, 2011, 36(1): 16–18
100. Ozcan A, Tewary A, Digonnet M J F, Kino G S. Observation of mode coupling in bitapered air-core photonic bandgap fibers. Optics Communications, 2007, 271(2): 391–395
101. Wang Y P, Jin W, Ju J, Xuan H F, Ho H L, Xiao L M, Wang D N. Long period gratings in air-core photonic bandgap fibers. Optics Express, 2008, 16(4): 2784–2790
102. Jin L, Jin W, Ju J, Wang Y P. Investigation of long-period grating resonances in hollow-core photonic bandgap fibers. Journal of Lightwave Technology, 2011, 29(11): 1708–1714
103. Xuan H F, Jin W, Ju J, Wang Y P, Zhang M, Liao Y B, Chen M H. Hollow-core photonic bandgap fiber polarizer. Optics Letters, 2008, 33(8): 845–847
104. Hoo Y L, Jin W, Ho H L, Ji J, Wang D N. Gas diffusion measurement using hollow-core photonic bandgap fiber. Sensors and Actuators. B, Chemical, 2005, 105(2): 183–186
105. Hoo Y L, Liu S J, Ho H L, Jin W. Fast response microstructured optical fiber methane sensor with multiple side-openings. IEEE Photonics Technology Letters, 2010, 22(5): 296–298
106. Pang M, Jin W. Detection of acoustic pressure with hollow-core photonic bandgap fiber. Optics Express, 2009, 17(13): 11088–11097
107. Xiao L, Demokan M S, Jin W, Wang Y, Zhao C L. Fusion splicing photonic crystal fibers and conventional single-mode Fibers: microhole collapse effect. Journal of Lightwave Technology, 2007, 25(11): 3563–3574
108. Xiao L, Jin W, Demokan M S. Fusion splicing small-core photonic crystal fibers and single-mode fibers by repeated arc discharges. Optics Letters, 2007, 32(2): 115–117